Automatica 117 (2020) 108991

Contents lists available at ScienceDirect

Automatica

journal homepage: www.elsevier.com/locate/automatica

Hierarchical nonlinear control for multi-rotor asymptotic stabilization based on zero-moment direction☆

Giulia Michieletto [a,*], Angelo Cenedese [a], Luca Zaccarian [b,c], Antonio Franchi [d,b]

[a] Department of Information Engineering, University of Padova, Padova, Italy
[b] LAAS-CNRS, Université de Toulouse, CNRS, Toulouse, France
[c] Department of Industrial Engineering, University of Trento, Trento, Italy
[d] Department of Robotics and Mechatronics, University of Twente, Enschede, The Netherlands

ARTICLE INFO

Article history:
Received 21 March 2019
Received in revised form 17 January 2020
Accepted 18 March 2020
Available online 21 April 2020

Keywords:
UAVs
Nonlinear feedback control
Asymptotic stabilization
Lyapunov methods
Hovering

ABSTRACT

We consider the hovering control problem for a class of multi-rotor aerial platforms with generically oriented propellers, characterized by intrinsically coupled translational and rotational dynamics. In doing this, we first discuss some assumptions guaranteeing the rejection of generic disturbance torques while compensating for the gravity force. These assumptions are translated into a geometric condition usually satisfied by both standard models and more general configurations. Then, we propose a control strategy based on the identification of a zero-moment direction for the exerted force and a dynamic state feedback linearization based on this preferential direction, which locally asymptotically stabilizes the platform to a static hovering condition. Stability properties of the control law are rigorously proved through Lyapunov-based methods and reduction theorems for the stability of nested sets. Asymptotic zeroing of the error dynamics and convergence to the static hovering condition are then confirmed by simulation results on a star-shaped hexarotor model with tilted propellers.

1. Introduction

In recent years, technological advances in miniaturized sensors/actuators and optimized data processing have lead to extensive use of small autonomous flying vehicles within the academic, military, and commercial contexts (Fuhrmann & Horowitz, 2017; Shakhatreh et al., 2019; Tang & Kumar, 2018). Thanks to their high maneuverability and versatility, Unmanned Aerial Vehicles (UAVs) are rapidly increasing in popularity, thus becoming a mature technology in several application fields ranging from the classical visual sensing tasks (e.g., surveillance and aerial photography (Kim, Mokdad, & Ben-Othman, 2018; Motlagh, Bagaa, & Taleb, 2017)) to the recent environment exploration and physical interaction (e.g., search-and-rescue operations, grasping and manipulation (Hayat, Yanmaz, Brown, & Bettstetter, 2017; Loianno et al., 2018; Ollero et al., 2018; Ruggiero, Lippiello, & Ollero, 2018; Spurnỳ et al., 2019)).

In most of these frameworks, the vehicle is required to stably hover at a fixed position and many control strategies exists for UAV, solving this hovering stabilization goal. These controllers are generally linear solutions based on proportional–derivative schemes or linear quadratic regulators, see, e.g., Alkhoori, Safwan, Zweiri, Sahinkaya, and Seneviratne (2017), Liu, Pan, and Chang (2016) and Sandiwan, Cahyadi, and Herdjunanto (2017). Hovering nonlinear controllers are instead not equally popular and mainly exploit feedback linearization (Antonello, Michieletto, Antonello, & Cenedese, 2018; Lotufo, Colangelo, Perez-Montenegro, Novara, & Canuto, 2016), sliding mode and backstepping techniques (Abci, Zheng, Efimov, & El Najjar, 2017; Chen, Jiang, Zhang, Jiang, & Tao, 2016) and/or geometric approaches (Franchi, Carli, Bicego, & Ryll, 2018; Invernizzi & Lovera, 2017).

Although less used, the effectiveness of nonlinear hovering control schemes has been widely confirmed by experimental tests. For example, the performance of controllers based on nested saturations, backstepping and sliding modes has been experimentally evaluated in Carrillo, Dzul, and Lozano (2012) to stabilize the position of a quadrotor w.r.t. a visual landmark on the ground. Similarly, in Choi and Ahn (2015) a quadrotor platform has been used to validate the possibility of stably tracking a point through

☆ This work has been partially funded by the European Union's Horizon 2020 research and innovation program under grant agreement No 871479 AERIAL-CORE; by the LAAS-CNRS under the grant GRASP and Carnot project; by the University of Padova under grant agreement BIRD168152, and by ANR via grant HANDY, No ANR-18-CE40-0010. The material in this paper was partially presented at the 20th IFAC World Congress of the International Federation of Automatic Control, July 9–14, 2017, Toulouse, France. This paper was recommended for publication in revised form by Associate Editor Angelo Alessandri under the direction of Editor Thomas Parisini.

* Corresponding author.
E-mail addresses: giulia.michieletto@unipd.it (G. Michieletto), angelo.cenedese@unipd.it (A. Cenedese), luca.zaccarian@laas.fr (L. Zaccarian), antonio.franchi@laas.fr (A. Franchi).

https://doi.org/10.1016/j.automatica.2020.108991
0005-1098/

a nonlinear control strategy that exploits a backstepping-like feedback linearization method. Likewise, the experimental results reported in Goodarzi and Lee (2017) confirm the performance of a geometric nonlinear controller during the autonomous tracking of a Lissajous curve employing a small quadrotor.

An overview of feedback control laws for underactuated UAVs is given in Hua, Hamel, Morin, and Samson (2013), where the authors claim that nonlinear controllers can also be endowed with provable global stability and convergence properties, under some suitable assumptions. In this spirit, Lyapunov theory has been exploited in Lee, Leoky, and McClamroch (2010) to prove the convergence of the proposed (nonlinear) tracking controller assuming bounded initial errors. The corresponding solution exploits a geometric approach on the three-dimensional Special Euclidean manifold and ensures almost global exponential convergence to zero of the tracking error. A Lyapunov-based approach is used also in Franchi et al. (2018) to verify the stability of a pose controller for the class of laterally-bounded force aerial vehicles, which includes both underactuated and fully actuated systems with saturation.

In this context, the contribution of our work can be summarized as follows. First, we account for a class of multi-rotor aerial platforms having more complex dynamics than the standard quadrotors. More specifically, we address the case where the propellers are in any number (possibly larger than four) and their spinning axes are generically oriented (including the non-parallel case). This entails the fact that the direction along which the control force is exerted is not necessarily orthogonal to the plane containing all the propellers centers[1] and that the control moment is not completely independent of the control force, as in the typical frameworks, see, e.g., Lee et al. (2010). For such generic platforms, we propose a nonlinear hovering control law that rests upon the identification of a so-called *zero-moment direction*. This concept, introduced in Michieletto, Ryll and Franchi (2017) and Michieletto, Ryll, and Franchi (2018), refers to a virtual direction along which the intensity of the control force can be freely assigned while retaining a zero control moment. Our controller exploits a dynamic feedback linearization scheme exploiting this preferential direction, which can be generically oriented (contrarily to the state-of-the-art multi-rotor controllers). Its implementation asymptotically stabilizes the platform to a given constant reference position, constraining its linear and angular velocities to be zero (*static hover condition* (Michieletto et al., 2018)). The proposed control strategy requires some algebraic prerequisites on the control matrices that map the motors inputs to the vehicle control force and moment. These are fulfilled by the majority of quadrotor models and result to be non-restrictive so that the designed controller can be applied to both standard multi-rotor platforms, whose propellers' spinning axes are all parallel, and more general ones. The local stability and convergence properties of our control law are confirmed by the numerical simulations and are rigorously proved through a Lyapunov-based proof using reduction theorems for the stability of nested sets. This work generalizes and extends (Michieletto, Cenedese, Zaccarian & Franchi, 2017). In particular, as compared to those preliminary results, we state a more appealing version of our basic assumptions, we extend our control goal including a restricted orientation stabilization feature, we provide proofs that were previously missing and we discuss new simulation tests better illustrating the benefits of our solution.

The rest of the paper is organized as follows. Since we use the unit quaternion representation of the attitude, in Section 2 some basic notions on the related mathematics are given. In Section 3 the dynamic model of a generic multi-rotor UAV is derived, exploiting the Newton–Euler approach. In Section 4 we state our main assumption on the allowable propellers configuration providing a set of necessary and sufficient conditions. Our control law is described in Section 5 and its stability properties are characterized in Section 6. The validity of our controller is illustrated through numerical simulations in Section 7. In Section 8 some conclusions are drawn and future research directions are discussed.

[1] This is strictly valid for standard star-shaped or H-shaped configurations, while for the Y-shaped case and other ones this idea can be easily generalized.

2. Preliminaries and notation

In this work, the unit quaternion formalism is adopted to represent the UAV attitude, overcoming the singularities that characterize Euler angles and simplifying the equations w.r.t. the rotation matrices representation. To provide a mathematical background for the model and the controller described hereafter, the main properties of unit quaternions are recalled in this section. The reader is referred to Diebel (2006) and Kuipers (2002) for further details.

A unit quaternion $\mathbf{q}$ is a hyper-complex number belonging to the unit hypersphere $\mathbb{S}^3$ embedded in $\mathbb{R}^4$. This is usually represented as a four dimensional vector having unitary norm made up of a scalar part, $\eta \in \mathbb{R}$, and a vector part, $\boldsymbol{\epsilon} \in \mathbb{R}^3$, so that $\mathbf{q} := \begin{bmatrix} \eta & \boldsymbol{\epsilon}^\top \end{bmatrix}^\top$ with $\|\mathbf{q}\|^2 = \eta^2 + \|\boldsymbol{\epsilon}\|^2 = 1$. Each unit quaternion $\mathbf{q}$ corresponds to a unique rotation matrix belonging to the Special Orthogonal group $SO(3) := \{\mathbf{R} \in \mathbb{R}^{3\times 3} \mid \mathbf{R}^\top\mathbf{R} = \mathbf{I}_3,\ \det(\mathbf{R}) = 1\}$. Formally, this is

$$\begin{aligned}\mathbf{R}(\mathbf{q}) &= \mathbf{I}_3 + 2\eta[\boldsymbol{\epsilon}]_\times + 2[\boldsymbol{\epsilon}]_\times^2 \\ &= \mathbf{I}_3 + 2\eta[\boldsymbol{\epsilon}]_\times + 2(\boldsymbol{\epsilon}\boldsymbol{\epsilon}^\top - \boldsymbol{\epsilon}^\top\boldsymbol{\epsilon}\mathbf{I}_3),\end{aligned} \tag{1}$$

where the operator $[\cdot]_\times$ denotes the map that associates any non-zero vector in $\mathbb{R}^3$ to the related skew-symmetric matrix in the special orthogonal Lie algebra $\mathfrak{so}(3)$. Thanks to (1), it can be verified that $\mathbf{R}(\mathbf{q})^\top\mathbf{R}(\mathbf{q}) = \mathbf{R}(\mathbf{q}_I) = \mathbf{I}_3$ where $\mathbf{q}_I := \begin{bmatrix} 1 & 0 & 0 & 0 \end{bmatrix}^\top$ is the *identity* (unit) quaternion.

The claimed relationship about the attitude representations is not bijective since each rotation matrix corresponds to two unit quaternions. To explain this fact, it is convenient to consider the following axis-angle representation for a unit quaternion, i.e.,

$$\mathbf{q} = \mathfrak{q}(\delta, \mathbf{n}) := \begin{bmatrix} \cos\left(\frac{\delta}{2}\right) & \sin\left(\frac{\delta}{2}\right)\mathbf{n}^\top \end{bmatrix}^\top, \tag{2}$$

where $\mathbf{n} \in \mathbb{S}^2$ is the rotation axis in $\mathbb{R}^3$ and $\delta \in (-\pi, +\pi]$ is the rotation angle. Using this expression, it can be verified that a rotation around $-\mathbf{n}$ of an angle $-\delta$ is described by the same unit quaternion associated with a rotation by δ about $\mathbf{n}$, namely $\mathbf{R}(\mathbf{q}) = \mathbf{R}(-\mathbf{q})$, the so-called *double coverage property*.

In quaternion-based algebra, compositions are performed through the *quaternions product*, denoted hereafter by the symbol $\circ$. Specifically, given $\mathbf{q}_1, \mathbf{q}_2$, it holds that $\mathbf{R}(\mathbf{q}_1)\mathbf{R}(\mathbf{q}_2) = \mathbf{R}(\mathbf{q}_3)$, where

$$\mathbf{q}_3 := \mathbf{q}_1 \circ \mathbf{q}_2 = \mathbf{A}(\mathbf{q}_1)\mathbf{q}_2 = \mathbf{B}(\mathbf{q}_2)\mathbf{q}_1, \quad \text{with} \tag{3}$$

$$\mathbf{A}(\mathbf{q}) := \begin{bmatrix} \eta & -\boldsymbol{\epsilon}^\top \\ \boldsymbol{\epsilon} & \eta\mathbf{I}_3 + [\boldsymbol{\epsilon}]_\times \end{bmatrix}, \quad \mathbf{B}(\mathbf{q}) := \begin{bmatrix} \eta & -\boldsymbol{\epsilon}^\top \\ \boldsymbol{\epsilon} & \eta\mathbf{I}_3 - [\boldsymbol{\epsilon}]_\times \end{bmatrix}. \tag{4}$$

According to (3), the inverse of a quaternion $\mathbf{q}$ may be chosen as $\mathbf{q}^{-1} = [\eta \ \ -\boldsymbol{\epsilon}^\top]^\top \in \mathbb{S}^3$. Given two 3D coordinate systems $\mathscr{F}_x$ and $\mathscr{F}_y$ such that the unit quaternion $\mathbf{q}$ indicates the relative rotation from $\mathscr{F}_x$ to $\mathscr{F}_y$, for any vector $\mathbf{w}_x \in \mathbb{R}^3$ expressed in $\mathscr{F}_x$ the corresponding vector $\mathbf{w}_y \in \mathbb{R}^3$ in $\mathscr{F}_y$ is computed as $\begin{bmatrix} 0 & \mathbf{w}_y^\top \end{bmatrix}^\top = \mathbf{q} \circ \begin{bmatrix} 0 & \mathbf{w}_x^\top \end{bmatrix}^\top \circ \mathbf{q}^{-1}$. The time derivative of a unit quaternion $\mathbf{q}$ is given by

$$\dot{\mathbf{q}} = \frac{1}{2}\mathbf{q} \circ \begin{bmatrix} 0 \\ \boldsymbol{\omega} \end{bmatrix} = \frac{1}{2}\mathbf{A}(\mathbf{q})\begin{bmatrix} 0 \\ \boldsymbol{\omega} \end{bmatrix} = \frac{1}{2}\begin{bmatrix} -\boldsymbol{\epsilon}^\top \\ \eta\mathbf{I}_3 + [\boldsymbol{\epsilon}]_\times \end{bmatrix}\boldsymbol{\omega}, \tag{5}$$

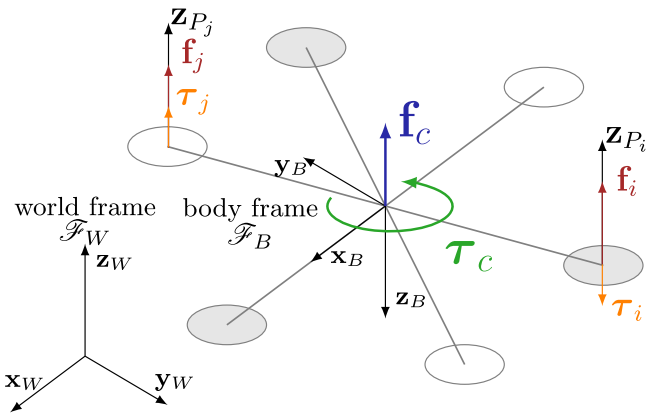

Fig. 1. Sample Generically Tilted Multi-Rotor having $n = 6$ CCW (gray) and CW (white) propellers, characterized by all parallel spinning axes.

denoting by $\boldsymbol{\omega} \in \mathbb{R}^3$ the angular velocity of $\mathscr{F}_x$ w.r.t. $\mathscr{F}_y$ expressed in $\mathscr{F}_x$. Relation (5) should be replaced by

$$\dot{\mathbf{q}} = \frac{1}{2}\begin{bmatrix} 0 \\ \boldsymbol{\omega}' \end{bmatrix} \circ \mathbf{q} = \frac{1}{2}\mathbf{B}(\mathbf{q})\begin{bmatrix} 0 \\ \boldsymbol{\omega}' \end{bmatrix} = \frac{1}{2}\begin{bmatrix} -\boldsymbol{\epsilon}^\top \\ \eta \mathbf{I}_3 - [\boldsymbol{\epsilon}]_\times \end{bmatrix}\boldsymbol{\omega}', \tag{6}$$

when the angular velocity is expressed in $\mathscr{F}_y$, namely $\boldsymbol{\omega}' = \mathbf{R}(\mathbf{q})\boldsymbol{\omega}$.

3. Dynamic model and problem statement

Consider a generic aerial multi-rotor platform, composed by a rigid body and $n \geq 4$ propellers (with negligible mass and moment of inertia w.r.t. the body inertial parameters), each one spinning about a generically oriented axis. The relative axes orientations, jointly with the number n of rotors, determines if the UAV is an underactuated or a fully actuated system (Ryll et al., 2019). This class of vehicles (also known as *Generically Tilted Multi-Rotors*) has been evaluated for the first time in Michieletto, Ryll et al. (2017), nonetheless, we investigate here the derivation of the dynamic model by exploiting the unit quaternion formalism to represent the attitude of the platform.

As reported in Fig. 1, we consider the *body frame* $\mathscr{F}_B = \{O_B, (\mathbf{x}_B, \mathbf{y}_B, \mathbf{z}_B)\}$ attached to the UAV so that its origin O_B coincides with the center of mass (CoM) of the vehicle. The pose of the platform in the inertial *world frame* $\mathscr{F}_W = \{O_W, (\mathbf{x}_W, \mathbf{y}_W, \mathbf{z}_W)\}$ is, thus, described by pair $(\mathbf{p}, \mathbf{q}) \in \mathbb{R}^3 \times \mathbb{S}^3$ where vector $\mathbf{p} \in \mathbb{R}^3$ denotes the position of O_B in $\mathscr{F}_W$ and the unit quaternion $\mathbf{q} \in \mathbb{S}^3$ represents the orientation of $\mathscr{F}_B$ w.r.t. $\mathscr{F}_W$ (i.e., it corresponds to the relative rotation from body to world frame, hence its inverse provides the coordinates in body frame of a vector expressed in the world frame). The orientation kinematics of the vehicle is governed by (5), where $\boldsymbol{\omega} \in \mathbb{R}^3$ represents the angular velocity of $\mathscr{F}_B$ w.r.t. $\mathscr{F}_W$, expressed in $\mathscr{F}_B$, whereas the linear velocity of O_B in $\mathscr{F}_W$ is denoted by $\mathbf{v} = \dot{\mathbf{p}} \in \mathbb{R}^3$.

The ith propeller, $i \in \{1 \dots n\}$, rotates with angular velocity $\boldsymbol{\omega}_i \in \mathbb{R}^3$ about its spinning axis, which passes through the rotor center O_{P_i}. The position $\mathbf{p}_i \in \mathbb{R}^3$ of O_{P_i} and the direction of $\boldsymbol{\omega}_i$ are assumed to be constant in $\mathscr{F}_B$. The propeller angular velocity can thus be expressed as $\boldsymbol{\omega}_i := \omega_i \mathbf{z}_{P_i}$ where $\omega_i \in \mathbb{R}$ indicates the (controllable) rotor spinning rate and $\mathbf{z}_{P_i} \in \mathbb{S}^2$ is a unit vector parallel to the rotor spinning axis. While rotating, each propeller exerts a *thrust/lift force* $\mathbf{f}_i \in \mathbb{R}^3$ and a *drag moment* $\boldsymbol{\tau}_i \in \mathbb{R}^3$, both oriented along the direction defined by $\mathbf{z}_{P_i}$ and exerted at O_{P_i}. According to the most commonly acknowledged model, these two quantities are related to the rotor rate ω_i by way of

$$\mathbf{f}_i = \sigma c_{f_i} |\omega_i| \omega_i \mathbf{z}_{P_i} \quad \text{and} \quad \boldsymbol{\tau}_i = -c^+_{\tau_i} |\omega_i| \omega_i \mathbf{z}_{P_i}, \tag{7}$$

where $c_{f_i}, c^+_{\tau_i} > 0$ and $\sigma \in \{-1, 1\}$ are constant parameters depending on the propeller shape. The propeller is of counter-clockwise (CCW) type if $\sigma = 1$ and of clockwise (CW) type if $\sigma = -1$. The thrust of CCW propellers has the same direction as the angular velocity vector, whereas those are opposite for the CW case; the drag moment, instead, is always oppositely oriented w.r.t. $\boldsymbol{\omega}_i$.

Introducing $u_i := \sigma |\omega_i| \omega_i \in \mathbb{R}$ and $c_{\tau_i} := -\sigma c^+_{\tau_i} \in \mathbb{R}$, relations (7) can be rewritten as

$$\mathbf{f}_i = c_{f_i} u_i \mathbf{z}_{P_i} \quad \text{and} \quad \boldsymbol{\tau}_i = c_{\tau_i} u_i \mathbf{z}_{P_i}. \tag{8}$$

The sum of all the propeller forces coincides with the *control force* $\mathbf{f}_c \in \mathbb{R}^3$ exerted at the platform CoM, while the *control moment* $\boldsymbol{\tau}_c \in \mathbb{R}^3$ is the sum of the moment contributions due to both the thrust forces and the drag moments. These can be expressed in $\mathscr{F}_B$ as

$$\mathbf{f}_c = \textstyle\sum_{i=1}^n \mathbf{f}_i = \sum_{i=1}^n c_{f_i} \mathbf{z}_{P_i} u_i, \tag{9}$$

$$\boldsymbol{\tau}_c = \textstyle\sum_{i=1}^n (\mathbf{p}_i \times \mathbf{f}_i + \boldsymbol{\tau}_i) = \sum_{i=1}^n (c_{f_i} \mathbf{p}_i \times \mathbf{z}_{P_i} + c_{\tau_i} \mathbf{z}_{P_i}) u_i. \tag{10}$$

Defining the *control input vector* $\mathbf{u} = \begin{bmatrix} u_1 & \dots & u_n \end{bmatrix}^\top \in \mathbb{R}^n$, (9) and (10) can be written compactly as

$$\mathbf{f}_c = \mathbf{F}\mathbf{u} \quad \text{and} \quad \boldsymbol{\tau}_c = \mathbf{M}\mathbf{u}, \tag{11}$$

where $\mathbf{F}, \mathbf{M} \in \mathbb{R}^{3 \times n}$ are the *control force input matrix* and the *control moment input matrix*, respectively. Note that, since $c_{f_i} > 0$ and $c^+_{\tau_i} > 0$, none of the columns of both $\mathbf{F}$ and $\mathbf{M}$ is a zero vector, and therefore we have both $1 \leq \text{rk}(\mathbf{F}) \leq 3$ and $1 \leq \text{rk}(\mathbf{M}) \leq 3$ by construction.

Using the Newton–Euler approach and neglecting second order effects (e.g., the propeller gyroscopic effects), the dynamics of the multi-rotor vehicle is approximated by the following set of equations

$$\begin{cases} \dot{\mathbf{p}} = \mathbf{v} & \text{(a)} \\ \dot{\mathbf{q}} = \frac{1}{2}\mathbf{q} \circ \begin{bmatrix} 0 \\ \boldsymbol{\omega} \end{bmatrix} & \text{(b)} \\ m\dot{\mathbf{v}} = -mg\mathbf{e}_3 + \mathbf{R}(\mathbf{q})\mathbf{F}\mathbf{u} & \text{(c)} \\ \mathbf{J}\dot{\boldsymbol{\omega}} = -\boldsymbol{\omega} \times \mathbf{J}\boldsymbol{\omega} + \mathbf{M}\mathbf{u} & \text{(d)} \end{cases} \tag{12}$$

where $m > 0$ is the platform mass, $g > 0$ is the gravitational constant, and $\mathbf{e}_i \in \mathbb{R}^3$ with $i \in \{1, 2, 3\}$ is the ith column of the identity matrix in $\mathbb{R}^{3 \times 3}$. The positive definite constant matrix $\mathbf{J} \in \mathbb{R}^{3 \times 3}$ is the vehicle inertia in $\mathscr{F}_B$. Model (12)(a)–(12)(d) describes a nonlinear plant

$$\dot{\mathbf{x}}_p = f_p(\mathbf{x}_p, \mathbf{u}), \tag{13}$$

whose state is $\mathbf{x}_p := [\mathbf{p}^\top \mathbf{q}^\top \mathbf{v}^\top \boldsymbol{\omega}^\top]^\top \in \mathbb{R}^3 \times \mathbb{S}^3 \times \mathbb{R}^6$.

In this paper, we design a nonlinear control law to stabilize in static hovering conditions the multi-rotor platform (13) by solving the following problem.

Problem 1. Given the plant (13), corresponding to (12)(a)–(12)(d), find a dynamic state feedback controller

$$\dot{\mathbf{x}}_c = f_c(\mathbf{x}_c, \mathbf{x}_p, \mathbf{p}_r), \quad \mathbf{u} = h_c(\mathbf{x}_c, \mathbf{x}_p, \mathbf{p}_r) \tag{14}$$

that, for any constant reference position $\mathbf{p}_r \in \mathbb{R}^3$, (locally) asymptotically stabilizes position $\mathbf{p}_r$ and some hovering orientation. More precisely, the closed-loop system (13)–(14) should be locally asymptotically stable to a suitable compact set where $\mathbf{p} = \mathbf{p}_r$, and $\mathbf{v}$ and $\boldsymbol{\omega}$ are both zero, while orientation $\mathbf{q}$ may be arbitrary but constant.

The arbitrariness of the orientation is fundamental for the feasibility of Problem 1, which is in general solvable only if certain steady-state attitudes are realized by the platform (*static*

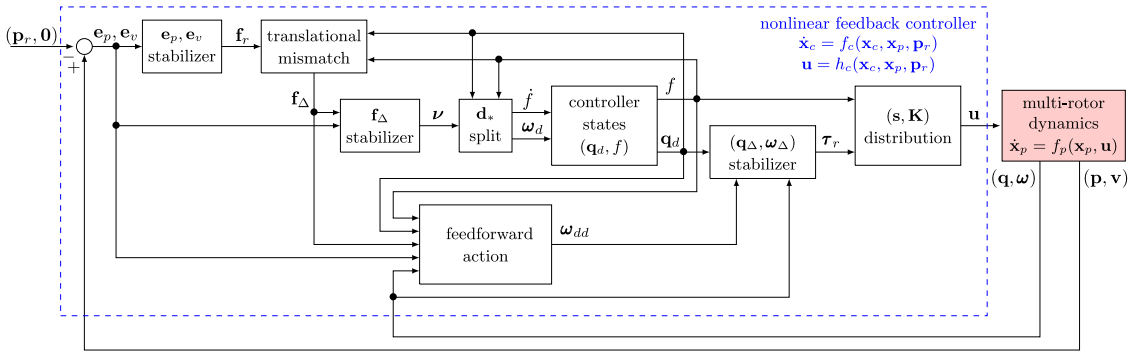

Fig. 2. Block diagram of the closed-loop system with the proposed dynamic control strategy.

hoverability realizability (Michieletto et al., 2018)). As compared to Michieletto, Cenedese et al. (2017), in Section 4 we provide new and more insightful sufficient conditions on matrices $\mathbf{F}$ and $\mathbf{M}$ in (11) for solving Problem 1, which is a contribution of this extension. Then, Section 5, presents the dynamics of the proposed control scheme, represented in Fig. 2. This controller architecture is a contribution of our preliminary work (Michieletto, Cenedese et al., 2017). On the other hand, Section 6 provides additional contributions of this improved version: first we provide a rigorous proof of local asymptotic stability of the error dynamics, by exploiting a hierarchical structure and the reduction theorems presented in El-Hawwary and Maggiore (2013); then, we propose an extension of the proposed control law, accounting also for the restricted stabilization of a given constant orientation.

4. Zero-moment preferential direction

4.1. Main assumption and zero-moment direction $\mathbf{d}_*$

In order to attain a constant position and orientation for the platform, the stabilizing controller must be able to simultaneously reject moment disturbances in any direction and counteract the gravity force. These requirements are satisfied under the next assumption on the control input matrices $\mathbf{F}$ and $\mathbf{M}$ introduced in (11) and on certain arbitrary bases of their kernels, namely

$$\bar{\mathbf{F}} \in \mathbb{R}^{n\times(n-\mathrm{rk}(\mathbf{F}))} \text{ such that } \mathrm{Im}(\bar{\mathbf{F}}) = \ker(\mathbf{F}), \tag{15}$$

$$\bar{\mathbf{M}} \in \mathbb{R}^{n\times(n-\mathrm{rk}(\mathbf{M}))} \text{ such that } \mathrm{Im}(\bar{\mathbf{M}}) = \ker(\mathbf{M}). \tag{16}$$

We emphasize that the properties of $\mathbf{F}$, $\mathbf{M}$, $\bar{\mathbf{F}}$ and $\bar{\mathbf{M}}$ discussed below are geometric properties of the subspaces $\ker(\mathbf{F})$ and $\ker(\mathbf{M})$ and are satisfied (or not) independently of the specific choices of $\bar{\mathbf{F}}$ and $\bar{\mathbf{M}}$ satisfying (15)–(16). We also highlight that a necessary condition for Assumption 1 to hold is that the UAV has at least 4 propellers. The proof of this fact is nontrivial and is given in Corollary 1 in Section 4.2.

Assumption 1. With $\bar{\mathbf{F}}$ as in (15), $rk(\mathbf{M}\bar{\mathbf{F}}) = 3$.

Assumption 1 implies $\mathrm{rk}(\mathbf{M}) = 3$ (matrix $\mathbf{M}$ has full row rank), corresponding to the possibility of freely assigning the control moment $\boldsymbol{\tau}_c$ in (11). Moreover, the condition $\mathrm{rk}(\mathbf{F}) \geq 1$ discussed after (11) ensures that there exists a zero moment direction generating a non-zero control force, as established below.[2]

Proposition 1. *Under Assumption 1, there exists* $\bar{\mathbf{u}} \in \ker(\mathbf{M})$ *such that* $\|\mathbf{F}\bar{\mathbf{u}}\| = 1$

[2] Differently from Michieletto et al. (2018), no constraint is imposed here on the positivity of the control input vector.

In view of Proposition 1, whose proof is postponed to Section 4.2 to avoid breaking the flow of the exposition, Assumption 1 enables a sufficient level of decoupling between $\mathbf{f}_c$ and $\boldsymbol{\tau}_c$ in (11), thus ensuring the existence of (at least) a direction where the intensity $\|\mathbf{f}_c\|$ of the control force can be arbitrarily assigned with the control moment $\boldsymbol{\tau}_c$ equal to zero. Referring to the notation in Michieletto et al. (2018), Assumption 1 is fulfilled for uncoupled platforms (UC) having at least a decoupled force direction (D1). Based on the quantity $\bar{\mathbf{u}}$ introduced in Proposition 1, this *zero-moment preferential direction* is defined as

$$\mathbf{d}_* := \mathbf{F}\bar{\mathbf{u}} \in \mathrm{Im}(\mathbf{F}) \cap \mathbb{S}^2. \tag{17}$$

We emphasize that Assumption 1 is more intuitive than (although equivalent to) the convoluted algebraic property introduced in our preliminary work (Michieletto, Cenedese et al., 2017). More specifically, we observe that Assumption 1 implies that $\mathbf{M}\bar{\mathbf{F}}$ is right-invertible, namely there exists a matrix $\mathbf{X} \in \mathbb{R}^{(n-\mathrm{rk}(\mathbf{F}))\times 3}$, whose dimensions depend on the rank of $\mathbf{F}$, such that $\mathbf{M}\bar{\mathbf{F}}\mathbf{X} = \mathbf{I}_3$. This corresponds to the property assumed in Michieletto, Cenedese et al. (2017) requiring the existence of a generalized right pseudo-inverse of $\mathbf{M}$, as stated next.

Lemma 1. *Assumption 1 holds if and only if there exists a matrix* $\mathbf{K} \in \mathbb{R}^{n\times n}$ *such that* $\mathbf{MKM}^\top$ *is invertible and* $\mathbf{F}\mathbf{M}_K^\dagger = \mathbf{0}$, *where* $\mathbf{M}_K^\dagger = \mathbf{KM}^\top(\mathbf{MKM}^\top)^{-1} \in \mathbb{R}^{n\times 3}$ *is the generalized right pseudo-inverse of* $\mathbf{M}$.

Proof. *(⇒)* We assume that $\mathrm{rk}(\mathbf{M}\bar{\mathbf{F}}) = 3$. Then, selecting $\mathbf{K} := \bar{\mathbf{F}}(\bar{\mathbf{F}})^\top$ we obtain from the rank condition that $\mathbf{MKM}^\top = \mathbf{M}\bar{\mathbf{F}}(\mathbf{M}\bar{\mathbf{F}})^\top \in \mathbb{R}^{3\times 3}$ is invertible. Moreover $\mathbf{F}\mathbf{M}_K^\dagger = \mathbf{0}$ because $\mathbf{F}\bar{\mathbf{F}} = \mathbf{0}$.

(⇐) Proceeding ab absurdo, we assume that $\mathrm{rk}(\mathbf{M}\bar{\mathbf{F}}) < 3$ and that a matrix $\mathbf{K}$ exists satisfying the properties in the statement of the lemma; for that matrix we have

$$\mathbf{F}\mathbf{M}_K^\dagger = \mathbf{0}, \quad \mathbf{M}\mathbf{M}_K^\dagger = \mathbf{I}. \tag{18}$$

Consider now any nonzero $\boldsymbol{\tau}_c \notin \mathrm{Im}(\mathbf{M}\bar{\mathbf{F}})$ (its existence is guaranteed by the stated rank assumption) and denote $\mathbf{u} := \mathbf{M}_K^\dagger\boldsymbol{\tau}_c$. Then the left equation in (18) implies that $\mathbf{u} \in \ker(\mathbf{F})$, i.e., there exists $\mathbf{w} \in \mathbb{R}^n$ such that $\mathbf{u} = \bar{\mathbf{F}}\mathbf{w}$. Using the right equation in (18), through simple substitutions, we get $\boldsymbol{\tau}_c = \mathbf{M}\mathbf{M}_K^\dagger\boldsymbol{\tau}_c = \mathbf{M}\mathbf{u} = \mathbf{M}\bar{\mathbf{F}}\mathbf{w}$, which clearly contradicts the assumption that $\boldsymbol{\tau}_c \notin \mathrm{Im}(\mathbf{M}\bar{\mathbf{F}})$, leading to an absurd and completing the proof. □

4.2. Proof of Proposition 1

The following lemma, of independent interest, holds true for any selection of the matrices in (15)–(16) and is useful to the end of proving Proposition 1.

Lemma 2. *The following are equivalent:*

(i) $rk(\mathbf{F}\bar{\mathbf{M}}) \geq 1$;
(ii) $\exists \bar{\mathbf{u}} \in \ker(\mathbf{M})$ *such that* $\|\mathbf{F}\bar{\mathbf{u}}\| = 1$.

Proof. *(i)* $\Rightarrow$ *(ii)*. Since $\mathrm{Im}(\bar{\mathbf{M}}) = \ker(\mathbf{M})$, one can always select a unit vector $\mathbf{u}^\star \in \ker(\mathbf{M})$ as a linear combination of the columns of $\bar{\mathbf{M}}$ and the rank condition ensures that $\mathbf{F}\mathbf{u}^\star \neq \mathbf{0}$. Choosing $\bar{\mathbf{u}} = \mathbf{u}^\star / \|\mathbf{F}\mathbf{u}^\star\|$ completes the proof.

(ii) $\Rightarrow$ *(i)*. Since $\bar{\mathbf{u}} \in \ker(\mathbf{M})$ we may write $\bar{\mathbf{u}} = \bar{\mathbf{M}}\mathbf{a}$ for some $\mathbf{a} \in \mathbb{R}^{n-\mathrm{rk}(\mathbf{M})}$. Since $1 = \|\mathbf{F}\bar{\mathbf{u}}\| = \|\mathbf{F}\bar{\mathbf{M}}\mathbf{a}\|$, then it follows that $\mathrm{rk}(\mathbf{F}\bar{\mathbf{M}}) \geq 1$. □

We are now ready to prove Proposition 1.

Proof of Proposition 1. By virtue of Lemma 2 it is enough to prove that Assumption 1 implies $rk(\mathbf{F}\bar{\mathbf{M}}) \geq 1$, which is done next. Ab absurdo, we assume that $\mathrm{rk}(\mathbf{F}\bar{\mathbf{M}}) = 0$, i.e., the product $\mathbf{F}\bar{\mathbf{M}}$ corresponds to the null matrix. This implies $\ker(\mathbf{M}) \subseteq \ker(\mathbf{F})$, namely, $\ker(\mathbf{M}) \cap \ker(\mathbf{F}) = \ker(\mathbf{M})$. We recall that for generic matrices $\mathbf{A}$ and $\mathbf{B}$ of suitable dimensions it holds that $\mathrm{rk}(\mathbf{AB}) = \dim(\mathrm{Im}(\mathbf{AB})) = \mathrm{rk}(\mathbf{B}) - \dim(\ker(\mathbf{A}) \cap \mathrm{Im}(\mathbf{B}))$ (Zhang, 2011). Since $\mathrm{rk}(\mathbf{M}) = 3$ from Assumption 1, it follows that

$$\begin{aligned}\mathrm{rk}(\mathbf{M}\bar{\mathbf{F}}) &= \mathrm{rk}(\bar{\mathbf{F}}) - \dim\left(\ker(\mathbf{M}) \cap \mathrm{Im}(\bar{\mathbf{F}})\right)\\ &= \dim\left(\ker(\mathbf{F})\right) - \dim\left(\ker(\mathbf{M})\right)\\ &= n - \mathrm{rk}(\mathbf{F}) - (n - \mathrm{rk}(\mathbf{M}))\\ &= 3 - \mathrm{rk}(\mathbf{F}).\end{aligned}$$

Under Assumption 1, this gives $\mathrm{rk}(\mathbf{F}) = 0$, which contradicts the fact that $\mathbf{F}$ is non-zero by construction. □

A relatively interesting corollary of Lemma 2 is a rank property for the overall input matrix $[\mathbf{F}^\top \mathbf{M}^\top]^\top \in \mathbb{R}^{6\times n}$ which is not a priori assumed but is instead a consequence of Assumption 1.

Corollary 1. *Assumption 1 holds only if*
(i) the UAV has $n \geq 4$ propellers and
(ii) the control input matrices satisfy $rk([\mathbf{F}^\top \mathbf{M}^\top]^\top) \geq 4$.

Proof. Since $[\mathbf{F}^\top \mathbf{M}^\top]^\top$ has n columns, then (ii) $\Rightarrow$ (i). Hence we only need to prove that Assumption 1 implies item (ii). Assumption 1 implies $\mathrm{rk}([\mathbf{F}^\top \mathbf{M}^\top]^\top) = \mathrm{rk}(\mathbf{M}) + \mathrm{rk}(\mathbf{F} - \mathbf{F}\mathbf{M}^\dagger\mathbf{M}) \geq 3$ (Tian, 2004). Ab absurdo, suppose that $\mathrm{rk}([\mathbf{F}^\top \mathbf{M}^\top]^\top) = 3$, namely $\mathrm{rk}(\mathbf{F} - \mathbf{F}\mathbf{M}^\dagger\mathbf{M}) = 0$. Then $\mathbf{F} - \mathbf{F}\mathbf{M}^\dagger\mathbf{M} = \mathbf{0}$, but this contradicts the statement of Proposition 1, thus concluding the proof. □

5. Proposed dynamic controller

Based on Assumption 1 and its implications in Proposition 1, we propose here a dynamic controller where the control input $\mathbf{u}$ is selected as

$$\mathbf{u} = \mathbf{M}_K^\dagger \boldsymbol{\tau}_r + \bar{\mathbf{u}} f, \tag{19}$$

so that the *reference moment* $\boldsymbol{\tau}_r \in \mathbb{R}^3$ and *force intensity* $f \in \mathbb{R}$ conveniently appear in expression (11). Indeed, by Proposition 1 using the zero-moment direction in (17), selection (19) implies,

$$\mathbf{f}_c = \mathbf{F}\mathbf{u} = \mathbf{d}_* f, \tag{20}$$

$$\boldsymbol{\tau}_c = \mathbf{M}\mathbf{u} = \boldsymbol{\tau}_r, \tag{21}$$

which clearly reveals a favorable decoupling in the wrench components. Taking advantage of this decoupling, we are interested in steering the platform toward a *desired orientation* $\mathbf{q}_d \in \mathbb{S}^3$ such that the resulting force $\mathbf{R}(\mathbf{q}_d)\mathbf{f}_c$ acting on the translational dynamics (12)(c) (in the direction of $\mathbf{R}(\mathbf{q}_d)\mathbf{d}_*$ because of (20)) coincides with a desired stabilizing action selected here as a simple PD + gravity compensation feedback function $\mathbf{f}_r \in \mathbb{R}^3$ corresponding to

$$\mathbf{f}_r := mg\mathbf{e}_3 - k_{pp}\mathbf{e}_p - k_{pd}\mathbf{e}_v, \tag{22}$$

where $\mathbf{e}_p = \mathbf{p} - \mathbf{p}_r \in \mathbb{R}^3$ and $\mathbf{e}_v = \mathbf{v} \in \mathbb{R}^3$ are the *position error* and the *velocity error*, respectively, while $k_{pp}, k_{pd} \in \mathbb{R}^+$ are arbitrary (positive) scalar PD gains governing the proportional and derivative actions of the attitude transient. Rather than algebraically computing $\mathbf{q}_d$, an auxiliary state can be introduced in the controller, accounting for the evolution of $\mathbf{q}_d$ in $\mathbb{S}^3$ through the quaternion-based dynamics (5), namely

$$\dot{\mathbf{q}}_d = \frac{1}{2}\mathbf{q}_d \circ \begin{bmatrix} 0 \\ \boldsymbol{\omega}_d \end{bmatrix}, \tag{23}$$

where $\boldsymbol{\omega}_d \in \mathbb{R}^3$ is an additional virtual input to be selected so that the actual input to the translational dynamics (12)(c) converges to the state feedback (22). In other words, $\boldsymbol{\omega}_d$ should drive to zero the following mismatch, motivated by (12)(c) and (20),

$$\mathbf{f}_\Delta := \mathbf{R}(\mathbf{q}_d)\mathbf{f}_c - \mathbf{f}_r = \mathbf{R}(\mathbf{q}_d)\mathbf{d}_* f - \mathbf{f}_r. \tag{24}$$

We will ensure that $\mathbf{f}_\Delta$ converges to zero by considering the variable f in (19) as an additional scalar state of the controller, and then imposing

$$\boldsymbol{\omega}_d = \frac{1}{f}[\mathbf{d}_*]_\times \mathbf{R}(\mathbf{q}_d)^\top \boldsymbol{\nu}, \tag{25}$$

$$\dot{f} = (\mathbf{R}(\mathbf{q}_d)\mathbf{d}_*)^\top \boldsymbol{\nu}, \tag{26}$$

where

$$\boldsymbol{\nu} := \frac{k_{pd}k_{pp}}{m}\mathbf{e}_p + \left(\frac{k_{pd}^2}{m} - k_{pp}\right)\mathbf{e}_v - \left(\frac{k_{pd}}{m} + k_\Delta\right)\mathbf{f}_\Delta, \tag{27}$$

with $k_\Delta \in \mathbb{R}^+$ being an additional (positive) scalar gain. Note that Eq. (25) requires $f \neq 0$ (this is guaranteed by the stated assumptions and will be formally established in Fact 2 in Section 6.2).

The scheme is completed by an appropriate selection of $\boldsymbol{\tau}_r$ in (19) ensuring that the attitude $\mathbf{q}$ tracks the desired attitude $\mathbf{q}_d$. This task is easily realizable because of Assumption 1, which guarantees full-authority control action on the rotational dynamics. To simplify the exposition, we introduce the mismatch $\mathbf{q}_\Delta \in \mathbb{S}^3$ between the current and the desired orientation, namely

$$\mathbf{q}_\Delta := \mathbf{q}_d^{-1} \circ \mathbf{q} = \begin{bmatrix} \eta_d\eta + \boldsymbol{\epsilon}_d^\top\boldsymbol{\epsilon} \\ -\eta\boldsymbol{\epsilon}_d + \eta_d\boldsymbol{\epsilon} - [\boldsymbol{\epsilon}_d]_\times\boldsymbol{\epsilon} \end{bmatrix} = \begin{bmatrix} \eta_\Delta \\ \boldsymbol{\epsilon}_\Delta \end{bmatrix}. \tag{28}$$

Then moment $\boldsymbol{\tau}_r$ in (19) entailing the convergence to zero of this mismatch can be selected as

$$\boldsymbol{\tau}_r = -k_{ap}\boldsymbol{\epsilon}_\Delta - k_{ad}\boldsymbol{\omega}_\Delta + \boldsymbol{\omega} \times \mathbf{J}\boldsymbol{\omega} + \mathbf{J}\boldsymbol{\omega}_{dd}, \tag{29}$$

where $\boldsymbol{\omega}_\Delta = \boldsymbol{\omega} - \boldsymbol{\omega}_d \in \mathbb{R}^3$ is the angular velocity mismatch and the PD gains $k_{ap} \in \mathbb{R}^+$ and $k_{ad} \in \mathbb{R}^+$ allow to tune the proportional and derivative actions of the attitude transient, respectively.

Note that a feedforward term appears in (29), compensating for the quadratic terms in $\boldsymbol{\omega}$ emerging in (12)(d), in addition to a correction term $\boldsymbol{\omega}_{dd} \in \mathbb{R}^3$ ensuring forward invariance of the set where $\mathbf{q} = \mathbf{q}_d$ and $\boldsymbol{\omega} = \boldsymbol{\omega}_d$. The expression of this term is reported in (30), and can be proved to be equal to $\dot{\boldsymbol{\omega}}_d$ along the solutions (the proof is available in Appendix).

Eqs. (22)–(35) may be gathered in the dynamics $\dot{\mathbf{x}}_c = f_c(\mathbf{x}_c, \mathbf{x}_p, \mathbf{p}_r)$ of controller (14), represented by the dashed blue block in Fig. 2, whose state is $\mathbf{x}_c = \begin{bmatrix}\mathbf{q}_d^\top & f\end{bmatrix}^\top \in \mathbb{S}^3 \times \mathbb{R}$ and whose inputs are the *plant state vector* $\mathbf{x}_p$ introduced at the end of Section 3, and the reference position $\mathbf{p}_r \in \mathbb{R}^3$ (see Eqs. (30)–(35) in Box I).

$$\boldsymbol{\omega}_{dd} = \frac{1}{f}[\mathbf{d}_*]_\times \mathbf{R}^\top(\mathbf{q}_d)\left(k_1\mathbf{R}(\mathbf{q})\mathbf{d}_*\xi f + k_2(\mathbf{e}_p,\mathbf{e}_v,\mathbf{f}_\Delta)\mathbf{e}_p + k_3(\mathbf{e}_p,\mathbf{e}_v,\mathbf{f}_\Delta)\mathbf{e}_v + k_4(\mathbf{e}_p,\mathbf{e}_v,\mathbf{f}_\Delta)\mathbf{f}_\Delta\right), \quad \text{where} \tag{30}$$

$$k_1 = \frac{k_{pd}^2}{m^2} - \frac{k_{pp}}{m}, \tag{31}$$

$$k_2(\mathbf{e}_p,\mathbf{e}_v,\mathbf{f}_\Delta) = -\left(\frac{k_{pd}^2 k_{pp}}{m^2} + \frac{k_{pp}^2}{m} + \kappa(\mathbf{e}_p,\mathbf{e}_v,\mathbf{f}_\Delta)\,\frac{k_{pd}k_{pp}}{m}\right), \tag{32}$$

$$k_3(\mathbf{e}_p,\mathbf{e}_v,\mathbf{f}_\Delta) = -\left(\frac{k_{pd}^2 k_{pp}}{m^2} + \frac{k_{pp}^2}{m} + \kappa(\mathbf{e}_p,\mathbf{e}_v,\mathbf{f}_\Delta)\,\frac{k_{pd}k_{pp}}{m}\right), \tag{33}$$

$$k_4(\mathbf{e}_p,\mathbf{e}_v,\mathbf{f}_\Delta) = \frac{k_{pd}^2}{m^2} - \frac{k_{pp}}{m} + \frac{k_{pd}k_\Delta}{m} + k_\Delta^2 + \kappa(\mathbf{e}_p,\mathbf{e}_v,\mathbf{f}_\Delta)\left(\frac{k_{pd}}{m} + k_\Delta\right), \tag{34}$$

$$\kappa(\mathbf{e}_p,\mathbf{e}_v,\mathbf{f}_\Delta) = -\frac{2}{f}\mathbf{d}_*^\top\mathbf{R}(\mathbf{q}_d)^\top\left(\frac{k_{pd}k_{pp}}{m}\mathbf{e}_p + \left(\frac{k_{pd}^2}{m} - k_{pp}\right)\mathbf{e}_v - \left(\frac{k_{pd}}{m} + k_\Delta\right)\mathbf{f}_\Delta\right). \tag{35}$$

Box I.

Remark 1. The feedback interconnection between (13) and (14) provides a smooth vector field in the region where $f \neq 0$, evolving in a closed set comprising Cartesian products of Euclidean spaces and $\mathbb{S}^3$. Due to these regularity properties, the local asymptotic stability results reported in Section 6 enjoy a certain degree of robustness, whose details are reported in Goebel, Sanfelice, and Teel (2012) (Ch. 7), ensuring a graceful performance degradation in the presence of unmodeled phenomena such as sensor noise and actuator dynamics. These useful properties are numerically illustrated in Section 7.

6. Stability analysis

6.1. Reduction theorem and invariance principle

To suitably formalize and prove closed-loop stability, we summarize here some essential results and notation from El-Hawwary and Maggiore (2013). First, given a closed set $\mathcal{S}$, an *open neighborhood* $\mathcal{N}(\mathcal{S})$ of $\mathcal{S}$ is an open set such that $\mathcal{S} \subset \mathcal{N}(\mathcal{S})$. Given $\varepsilon > 0$, the ε ball around $\mathcal{S}$ is $\mathcal{B}_\varepsilon(\mathcal{S}) := \{\mathbf{x};\ |\ \min_{\mathbf{y}\in\mathcal{S}} \|\mathbf{y}-\mathbf{x}\| < \varepsilon\}$. Then, denote by $\varphi(t,\mathbf{x}_0)$ the (unique) solution to the closed loop (13)–(14) starting at $\mathbf{x}(0) = (\mathbf{x}_p(0),\mathbf{x}_c(0)) = \mathbf{x}_0$ and evaluated at time $t \in \mathbb{R}_{\geq 0}$. The following are some basic stability definitions from El-Hawwary and Maggiore (2013) and Maggiore, Sassano, and Zaccarian (2019).

Definition 1. *(Set Stability and Attractivity)* Given[3] a closed (not necessarily bounded) set Γ_1,

(i) Γ_1 is *stable* for (13)–(14) if for each $\varepsilon > 0$ there exists a neighborhood $\mathcal{N}(\Gamma_1)$ of Γ_1 such that all solutions starting in $\mathcal{N}(\Gamma_1)$ never leave $\mathcal{B}_\varepsilon(\Gamma_1)$;

(ii) Γ_1 is *(locally) attractive* for (13)–(14) if there exists a neighborhood $\mathcal{N}(\Gamma_1)$ such that all solutions starting in $\mathcal{N}(\Gamma_1)$ converge to Γ_1 and it is *globally attractive* if all solutions converge to Γ_1;

(iii) Γ_1 is *(locally, respectively, globally) asymptotically stable* for (13)–(14) if it is stable and (locally, respectively, globally) attractive for (13)–(14);

(iv) given a closed set $\Gamma_2 \supset \Gamma_1$, set Γ_1 is stable, (locally or globally) attractive or (locally or globally) asymptotically stable *relative to* Γ_2, if the properties (i), (ii), (iii) above hold with initial conditions restricted to the set Γ_2.

Given a compact set Γ_1 and a closed set $\Gamma_2 \supset \Gamma_1$, the set Γ_2 is *locally asymptotically stable near* Γ_1 for (13)–(14) if there exists $r > 0$ such that all solutions starting in $\mathcal{B}_r(\Gamma_1)$ converge to Γ_2 (local attractivity near Γ_1) and the following property holds: (local stability near Γ_1) for each $\varepsilon > 0$, there exists $\delta > 0$ such that for any $\bar{t} > 0$, all solutions starting from $\mathbf{x}_0 \in \mathcal{B}_\delta(\Gamma_1)$ satisfy $(\varphi(t,\mathbf{x}_0) \in \mathcal{B}_r(\Gamma_1),\ \forall t \leq \bar{t}) \Rightarrow \varphi(\bar{t},\mathbf{x}_0) \in \mathcal{B}_\varepsilon(\Gamma_2)$.

The reader is referred to El-Hawwary and Maggiore (2013) and Maggiore et al. (2019) for further details about Definition 1, nonetheless we recall here that (local) asymptotic stability of Γ_2 implies (local) asymptotic stability of Γ_2 near Γ_1 for any $\Gamma_1 \subset \Gamma_2$. The following result is the reduction theorem used in our proof, which is a corollary of Thm. 4.7 in Maggiore et al. (2019).

Proposition 2. *Consider three closed sets $\Gamma_1 \subset \Gamma_2 \subset \Gamma_3$ with Γ_1 compact. If (i) Γ_1 is locally asymptotically stable for (13)–(14) relative to Γ_2 and (ii) Γ_2 is locally asymptotically stable for (13)–(14) near Γ_1, relative to Γ_3, then Γ_1 is locally asymptotically stable for (13)–(14) relative to Γ_3.*

We also present below a formulation of the invariance principle corresponding to a corollary of Thm. 1 in Seuret, Prieur, Tarbouriech, Teel, and Zaccarian (2019) that will be useful in the proofs of Section 6.3.

Proposition 3. *Consider system $\dot{\boldsymbol{\xi}} = \mathbf{f}(\boldsymbol{\xi})$, $\boldsymbol{\xi} \in \Xi$, where $\mathbf{f}$ is continuous and Ξ is a closed set, and a compact set $\mathcal{A} \subset \Xi$. If there exists a scalar $r > 0$ and a continuously differentiable function V, positive definite w.r.t. $\mathcal{A}$ (namely zero in $\mathcal{A}$ and positive outside $\mathcal{A}$), such that*

$$\dot{V}(\boldsymbol{\xi}) := \langle \nabla V(\boldsymbol{\xi}), \mathbf{f}(\boldsymbol{\xi})\rangle \leq 0, \quad \forall \boldsymbol{\xi} \in \mathcal{B}_r(\mathcal{A}), \tag{36}$$

and such that no solution φ exists starting from $\boldsymbol{\xi}_0 \in \mathcal{B}_r(\mathcal{A})$ for which $V(\varphi(t,\boldsymbol{\xi}_0)) = V(\boldsymbol{\xi}_0) \neq 0$, then $\mathcal{A}$ is locally asymptotically stable for $\dot{\boldsymbol{\xi}} = \mathbf{f}(\boldsymbol{\xi})$.

Proof. The proof is a direct consequence of Seuret et al. (2019, Thm 1). Continuity of $\mathbf{f}$ and closedness of Ξ ensures that the dynamics satisfies the hybrid basic conditions of As. 6.5 in Goebel

[3] Note that in El-Hawwary and Maggiore (2013) forward invariance of Γ_1 is assumed. However, as noted in the generalizations discussed in Maggiore et al. (2019), this assumption is not necessary. Moreover, the definition of *stability near a set* is slightly different from the one given in El-Hawwary and Maggiore (2013) and coincides with the (equivalent) formulation in Maggiore et al. (2019).

et al. (2012). Since the dynamics is only continuous-time (corresponding to $\mathcal{D} = \emptyset$ and $G(\xi) = \emptyset$ in Thm. 1 in Seuret et al. (2019) then only (Seuret et al., 2019, eqn. (2)) needs to be checked, which is guaranteed by (36) for a continuously differentiable V. Finally, for a local version of Thm. 1 in Seuret et al. (2019), radial unboundedness is not necessary and the local proof follows exactly the same steps as Thm. 1 in Seuret et al. (2019) with all the bounds restricted to a sublevel set $\mathcal{E}_\mu := \{\boldsymbol{\xi} : V(\boldsymbol{\xi}) \leq \mu\}$ of V, with $\mu > 0$, satisfying $\mathcal{E}_\mu \subset \mathcal{B}_r(\mathcal{A})$. □

6.2. Error dynamics

We consider here the closed loop between plant dynamics $\dot{\mathbf{x}}_p = f_p(\mathbf{x}_p, \mathbf{u})$, as defined at the end of Section 3 and controller dynamics $\dot{\mathbf{x}}_c = f_c(\mathbf{x}_c, \mathbf{x}_p, \mathbf{p}_r)$ through the expression of $\mathbf{u}$ in (19), introduced and discussed in Section 5. In particular, we select in this section suitable error coordinates enabling the stability proof carried out below in Section 6.3. We start by characterizing the dynamics of the *orientation error* variable $\mathbf{q}_\Delta$ in (28) and of the associated *angular velocity mismatch* $\boldsymbol{\omega}_\Delta$. As long as $f \neq 0$, so that ω_d in (25) is well defined, we may write:

$$\dot{\mathbf{q}}_\Delta = \frac{1}{2}\mathbf{q}_\Delta \circ \begin{bmatrix} 0 \\ \boldsymbol{\omega}_\Delta \end{bmatrix}, \tag{37}$$

$$\mathbf{J}\dot{\boldsymbol{\omega}}_\Delta = -\boldsymbol{\omega} \times \mathbf{J}\boldsymbol{\omega} - \mathbf{J}\dot{\boldsymbol{\omega}}_d + \boldsymbol{\tau}_r = -k_{ap}\boldsymbol{\epsilon}_\Delta - k_{ad}\boldsymbol{\omega}_\Delta, \tag{38}$$

where we used (29) and the fact that $\dot{\boldsymbol{\omega}}_d = \boldsymbol{\omega}_{dd}$, as proven in Appendix. Moreover, to establish useful properties of the translational dynamics, we use the *translational error* vector $\mathbf{e}_t := \begin{bmatrix}\mathbf{e}_p^\top & \mathbf{e}_v^\top\end{bmatrix}^\top \in \mathbb{R}^6$, introduced after (22), which well characterizes the deviation from the reference position $\mathbf{p}_r$ and the reference linear velocity $\mathbf{v}_r = \mathbf{0}_3$. Combining (12)(c) with the definition of $\mathbf{f}_\Delta$ given in (24) the dynamics of $\mathbf{e}_t$ can be written as follows

$$\dot{\mathbf{e}}_p = \mathbf{e}_v \tag{39}$$

$$m\dot{\mathbf{e}}_v = -mg\mathbf{e}_3 + (\mathbf{R}(\mathbf{q}) - \mathbf{R}(\mathbf{q}_d))\mathbf{f}_c + \mathbf{f}_r + \mathbf{f}_\Delta. \tag{40}$$

A last mismatch variable that needs to be characterized is the (scalar) controller state f. To this end, combining (12)(c) with (20), we observe that the zero position error condition $\mathbf{e}_p = \mathbf{0}_3$ can only be reached if the state f, governed by (26), converges to mg. Nonetheless, instead of describing the error system in terms of the deviation $f - mg$, we prefer to use the redundant set of coordinates $\mathbf{f}_\Delta$ in (24) and the attitude $\mathbf{q} \in \mathbb{S}^3$ of the platform whose dynamics is described by (12)(b). This choice of (error) variables is motivated by the following fact.

Fact 1. *As long as $f \neq 0$, the dynamics of the forces mismatch $\mathbf{f}_\Delta$ in (24) is given by*

$$\dot{\mathbf{f}}_\Delta = -k_\Delta \mathbf{f}_\Delta. \tag{41}$$

Proof. Using its definition in (24), the dynamics of the *forces mismatch* $\mathbf{f}_\Delta$ in (24) is given by

$$\dot{\mathbf{f}}_\Delta = \mathbf{R}(\mathbf{q}_d)\mathbf{d}_*\dot{f} + \dot{\mathbf{R}}(\mathbf{q}_d)\mathbf{d}_* f - \dot{\mathbf{f}}_r \tag{42}$$

$$= \dot{\mathbf{f}}_{\Delta,1} + \dot{\mathbf{f}}_{\Delta,2} + \dot{\mathbf{f}}_{\Delta,3} \tag{43}$$

with the following quantities being well defined because $f \neq 0$ and derived by using the selections of $\boldsymbol{\omega}_d, \dot{f}$ in (25), (26), the expression of $\mathbf{f}_r$ in (22) and the relation $[[\boldsymbol{\epsilon}_1]_\times \boldsymbol{\epsilon}_2]_\times = [\boldsymbol{\epsilon}_1]_\times [\boldsymbol{\epsilon}_2]_\times - [\boldsymbol{\epsilon}_2]_\times [\boldsymbol{\epsilon}_1]_\times = \boldsymbol{\epsilon}_2\boldsymbol{\epsilon}_1^\top - \boldsymbol{\epsilon}_1\boldsymbol{\epsilon}_2^\top$:

$$\dot{\mathbf{f}}_{\Delta,1} = \mathbf{R}(\mathbf{q}_d)\mathbf{d}_*\dot{f} = (\mathbf{R}(\mathbf{q}_d)\mathbf{d}_*)\,(\mathbf{R}(\mathbf{q}_d)\mathbf{d}_*)^\top \boldsymbol{\nu} \tag{44}$$

$$= \mathbf{R}(\mathbf{q}_d)\mathbf{d}_*\mathbf{d}_*^\top \mathbf{R}(\mathbf{q}_d)^\top \boldsymbol{\nu} \tag{45}$$

$$\dot{\mathbf{f}}_{\Delta,2} = \dot{\mathbf{R}}(\mathbf{q}_d)\mathbf{d}_* f = \mathbf{R}(\mathbf{q}_d)[\boldsymbol{\omega}_d]_\times \mathbf{d}_* f \tag{46}$$

$$= -\mathbf{R}(\mathbf{q}_d)[\mathbf{d}_*]_\times [\mathbf{d}_*]_\times \mathbf{R}(\mathbf{q}_d)^\top \boldsymbol{\nu} \tag{47}$$

$$\dot{\mathbf{f}}_{\Delta,3} = -\dot{\mathbf{f}}_r = k_{pp}\dot{\mathbf{e}}_p + k_{pd}\dot{\mathbf{e}}_v \tag{48}$$

$$= k_{pp}\mathbf{e}_v + \frac{k_{pd}}{m}\left(-k_{pp}\mathbf{e}_p - k_{pd}\mathbf{e}_v + \mathbf{f}_\Delta\right). \tag{49}$$

Summing up the terms (45), (47) and (49), we get

$$\dot{\mathbf{f}}_\Delta = \boldsymbol{\nu} - \frac{k_{pd}k_{pp}}{m}\mathbf{e}_p - \left(\frac{k_{pd}^2}{m} - k_{pp}\right)\mathbf{e}_v + \frac{k_{pd}}{m}\mathbf{f}_\Delta, \tag{50}$$

and, finally, employing the definition of $\boldsymbol{\nu}$ in (27), we obtain (41). □

All the previously introduced error variables can be used to prove that the proposed control scheme solves Problem 1. To formalize this observation, rather than using coordinates $(\mathbf{x}_p, \mathbf{x}_c) = (\mathbf{p}, \mathbf{q}, \mathbf{v}, \boldsymbol{\omega}, \mathbf{q}_d, f) \in \mathbb{R}^3 \times \mathbb{S}^3 \times \mathbb{R}^6 \times \mathbb{S}^3 \times \mathbb{R}$, we consider the following equivalent coordinates for the error dynamics

$$\mathbf{z} := (\mathbf{q}_\Delta, \boldsymbol{\omega}_\Delta, \mathbf{f}_\Delta, \mathbf{e}_t, \mathbf{q}) \tag{51}$$

$$\in \mathcal{Z} := \mathbb{S}^3 \times \mathbb{R}^3 \times \mathbb{R}^3 \times \mathbb{R}^6 \times \mathbb{S}^3 \subseteq \mathbb{R}^{20}.$$

The ensuing error dynamics $\dot{\mathbf{z}} = f_z(\mathbf{z})$ is given by (37)–(40), (41) and (12)(b).

In the following, we restrict the attention to the next compact set (that results from the Cartesian product of compact sets)

$$\mathcal{Z}_0 := \big\{\mathbf{z} \in \mathcal{Z} \mid \mathbf{q}_\Delta = \mathbf{q}_I, \boldsymbol{\omega}_\Delta = \mathbf{0}, \mathbf{f}_\Delta = \mathbf{0}, \mathbf{e}_t = \mathbf{0}, \mathbf{R}(\mathbf{q})\mathbf{d}_* = \mathbf{e}_3\big\}, \tag{52}$$

capturing the requirements of Problem 1. In particular, if $\mathbf{z}$ approaches asymptotically $\mathcal{Z}_0$, then the desired position is asymptotically reached ($\mathbf{e}_t = \mathbf{0}$) with some constant orientation $\mathbf{q}$ ensuring that the selected zero-moment direction $\mathbf{d}_*$ is correctly aligned with the steady-state action $mg\mathbf{e}_3$, thus compensating for the gravity force. Before proceeding with the stability analysis, we establish a useful property of the compact set $\mathcal{Z}_0$.

Fact 2. *There exists a scalar $r > 0$ such that the controller state f is (uniformly) bounded away from zero in the set $\mathcal{B}_r(\mathcal{Z}_0)$.*

Proof. Since in $\mathcal{Z}_0$ we have $\mathbf{e}_t = \mathbf{0}$ and $\mathbf{f}_\Delta = \mathbf{0}$, then from (24) it follows that $\mathbf{d}_* f = mg\mathbf{R}^\top(\mathbf{q}_d)\mathbf{e}_3$. Taking norms on both sides and due to the property of rotation matrices, it holds that $|f| = mg > 0$ in $\mathcal{Z}_0$. Continuity of f and compactness of $\mathcal{Z}_0$ then implies the existence of $r > 0$ such that $|f| > \frac{mg}{2}$ in $\mathcal{B}_r(\mathcal{Z}_0)$. To prove this, assume by a contradiction that such an $r > 0$ does not exist. Then there exists a sequence of points arbitrarily close to $\mathcal{Z}_0$ where $|f| \leq \frac{mg}{2}$ and from these points we can extract a converging subsequence whose limit belongs to $\mathcal{Z}_0$ and satisfies (by continuity) $|f| \leq \frac{mg}{2}$, which contradicts $f = mg$, thus completing the proof. □

6.3. Proof of asymptotic stability

In this section we apply the reduction approach summarized in Section 6.1 to prove the following main result.

Theorem 1. *Consider the closed-loop system in Fig. 2 between plant (13) and controller (14). The compact set $\mathcal{Z}_0$ in (52) is locally asymptotically stable for the corresponding dynamics. In particular, controller (14) is a solution to Problem 1.*

The reduction-based proof is carried out by focusing on increasingly large nested sets, each of them characterized by a desirable behavior of certain components of the error dynamics state $\mathbf{z}$ in (51). These sets satisfy the inclusion $\mathcal{Z}_0 = \mathcal{Z}_q \subset \mathcal{Z}_f \subset \mathcal{Z}_a \subset \mathcal{Z}$ with $\mathcal{Z}_0$ and $\mathcal{Z}$ defined in (51) and (52), respectively, $\mathcal{Z}_a$ being the subset of $\mathcal{Z}$ where the attitude mismatch $(\mathbf{q}_\Delta, \boldsymbol{\omega}_\Delta)$

is null and $\mathcal{Z}_f$ being the subset of $\mathcal{Z}_a$ where the virtual input $\mathbf{f}_r$ in (22) is the actual input of the translational dynamics (12)(a), namely the force mismatch $\mathbf{f}_\Delta$ is null. More precisely,

$$\mathcal{Z}_a := \{\mathbf{z} \in \mathcal{Z} \mid \mathbf{q}_\Delta = \mathbf{q}_I,\ \boldsymbol{\omega}_\Delta = \mathbf{0}\}, \tag{53}$$

$$\mathcal{Z}_f := \{\mathbf{z} \in \mathcal{Z}_a \mid \mathbf{f}_\Delta = \mathbf{0}\}, \tag{54}$$

$$\mathcal{Z}_q := \left\{\mathbf{z} \in \mathcal{Z}_f \mid \mathbf{e}_t = \mathbf{0}\right\}. \tag{55}$$

We first establish that $\mathcal{Z}_0$ coincides with $\mathcal{Z}_q$. Then we exploit the reduction approach of Proposition 2 to hierarchically enlarge the set of allowable initial conditions in a sequence of nested lemmas.

Lemma 3. *Set $\mathcal{Z}_0$ in (52) and set $\mathcal{Z}_q$ in (55) coincide.*

Proof. It is immediate to see that any point in $\mathcal{Z}_0$ also belongs to $\mathcal{Z}_q$. Consider now any point in $\mathcal{Z}_q$. Since $\mathbf{q}_\Delta = \mathbf{q}_I$, then $\mathbf{q}_d = \mathbf{q}$. Together with $\mathbf{f}_\Delta = \mathbf{0}$ and $\mathbf{e}_t = \mathbf{0}$, this implies from (22) and (24) that $\mathbf{R}(\mathbf{q})\mathbf{d}_* f = \mathbf{f}_r = mg\mathbf{e}_3$, namely $|f| = mg$ and $\mathbf{R}(\mathbf{q})\mathbf{d}_* = \mathbf{e}_3$ thus proving that the point is also in $\mathcal{Z}_0$. □

Lemma 4. *Set $\mathcal{Z}_0$ is locally asymptotically stable relative to $\mathcal{Z}_f$ for the error dynamics.*

Proof. By virtue of Lemma 3 we may equivalently prove local asymptotic stability of $\mathcal{Z}_q$. To this end, consider dynamics (39)–(40) for initial conditions in $\mathcal{Z}_f$. Such dynamics corresponds to the situation of input $\mathbf{f}_r$ acting directly on the translational component of the plant (12)(c), which provides the following autonomous system:

$$\dot{\mathbf{e}}_p = \mathbf{e}_v, \quad m\dot{\mathbf{e}}_v = -k_{pp}\mathbf{e}_p - k_{pd}\mathbf{e}_v. \tag{56}$$

Consider the Lyapunov function candidate

$$V_p := \frac{1}{2}m\mathbf{e}_v^\top\mathbf{e}_v + \frac{1}{2}k_{pp}\mathbf{e}_p^\top\mathbf{e}_p, \tag{57}$$

which is clearly positive definite (w.r.t. the origin) and whose derivative along (56) corresponds to

$$\begin{aligned}\dot{V}_p &= m\mathbf{e}_v^\top\dot{\mathbf{e}}_v + k_{pp}\mathbf{e}_p^\top\dot{\mathbf{e}}_p \\ &= \mathbf{e}_v^\top(-k_{pp}\mathbf{e}_p - k_{pd}\mathbf{e}_v) + k_{pp}\mathbf{e}_p^\top\mathbf{e}_v = -k_{pd}\|\mathbf{e}_v\|^2,\end{aligned}$$

which is negative semi-definite. Due to the left equation in (56), no solution (either from the zero one) can evolve with $\mathbf{e}_v$ identically zero, therefore no solution keeps V_p constant and nonzero, and local asymptotic stability of the origin for dynamics (56) follows from Proposition 3 applied with $\mathcal{A} = \{\mathbf{0}\}$. Since (56) coincides with the error dynamics $\dot{\mathbf{z}} = f_z(\mathbf{z})$ restricted to $\mathcal{Z}_f$, and with the origin coinciding with $\mathcal{Z}_q$, the proof is completed. □

Lemma 5. *Set $\mathcal{Z}_0$ is locally asymptotically stable, relative to $\mathcal{Z}_a$, for the error dynamics.*

Proof. We prove the result by applying Proposition 2 with $\Gamma_1 = \mathcal{Z}_0$, $\Gamma_2 = \mathcal{Z}_f$ and $\Gamma_3 = \mathcal{Z}_a$. In particular, hypothesis (i) of Proposition 2 is proven by Lemma 4. Hypothesis (ii) is proven next by showing that $\mathcal{Z}_f$ is locally asymptotically stable for (13)–(14) near $\mathcal{Z}_0$, relative to $\mathcal{Z}_a$. To this end, consider the derivative of $\mathbf{f}_\Delta$, along dynamics (39)–(40) restricted to $\mathcal{Z}_a$ (so that, using $\mathbf{q}_\Delta = \mathbf{q}_I$, we may use $\mathbf{q} = \mathbf{q}_d$) and close to $\mathcal{Z}_0$ (so that, according to Fact 2 f is bounded away from zero). From Fact 1, this corresponds to $\dot{\mathbf{f}}_\Delta = -k_\Delta\mathbf{f}_\Delta$ in (41). Then positivity of k_Δ establishes exponential stability of $\mathcal{Z}_f$ near $\mathcal{Z}_0$ for the dynamics restricted to $\mathcal{Z}_a$, using the Lyapunov function $V_\Delta := \mathbf{f}_\Delta^\top\mathbf{f}_\Delta$. □

Lemma 6. *Set $\mathcal{Z}_0$ is locally asymptotically stable, relative to $\mathcal{Z}$, for the error dynamics, i.e., Theorem 1 holds.*

Proof. Theorem 1 holds under the main statement of the lemma because $\mathcal{Z}$ is the overall state for the error dynamics. Therefore local asymptotic stability relative to $\mathcal{Z}$ coincides with local asymptotic stability.

We prove the main statement of the lemma by applying Proposition 2 with $\Gamma_1 = \mathcal{Z}_0$, $\Gamma_2 = \mathcal{Z}_a$ and $\Gamma_3 = \mathcal{Z}$. In particular, hypothesis (i) of Proposition 2 is proven by Lemma 5. The proof is completed next by showing hypothesis (ii), namely that $\mathcal{Z}_a$ is locally asymptotically stable for (13)–(14) near $\mathcal{Z}_0$, relative to $\mathcal{Z}$. To this end, we focus the attention on the states $\mathbf{q}_\Delta$ and $\boldsymbol{\omega}_\Delta$ whose evolution near $\mathcal{Z}_0$ (where f is bounded away from zero as established in Fact 2) is autonomous and has been computed in (37)–(38). To establish asymptotic stability of $\mathcal{Z}_a$ it is enough to focus on the compact set $\mathcal{A} := \{(\mathbf{q}_\Delta, \boldsymbol{\omega}_\Delta) \in \mathbb{S}^3 \times \mathbb{R}^3 : \mathbf{q}_\Delta = \mathbf{q}_I, \boldsymbol{\omega}_\Delta = \mathbf{0}\}$ for (37)–(38). In particular, we apply Proposition 3 by defining the Lyapunov function candidate

$$V_a := 2k_{ap}(1 - \eta_\Delta) + \frac{1}{2}\boldsymbol{\omega}_\Delta^\top\mathbf{J}\boldsymbol{\omega}_\Delta, \tag{58}$$

which is positive definite w.r.t. $\mathcal{A}$, due to the fact that $|\eta_\Delta| \leq 1$ because $q_\Delta \in \mathbb{S}^3$ by the definition of $\mathcal{Z}$. The derivative of V_a along (37), (38) turns out to be

$$\dot{V}_a = -2k_{ap}\dot{\eta}_\Delta + \boldsymbol{\omega}_\Delta^\top\mathbf{J}\dot{\boldsymbol{\omega}}_\Delta \tag{59}$$

$$= k_{ap}\boldsymbol{\omega}_\Delta^\top\boldsymbol{\epsilon}_\Delta + \boldsymbol{\omega}_\Delta^\top(-k_{ap}\boldsymbol{\epsilon}_\Delta - k_{ad}\boldsymbol{\omega}_\Delta) \tag{60}$$

$$= -k_{ad}\|\boldsymbol{\omega}_\Delta\|^2. \tag{61}$$

From standard Lyapunov-based attitude control (see, e.g., Mayhew, Sanfelice, and Teel (2009)) the only solution to (37)–(38) associated to a constant and nonzero V_a is the constant solution starting at $(\mathbf{q}_\Delta(0), \boldsymbol{\omega}_\Delta(0)) = (-\mathbf{q}_I, \mathbf{0})$, which is an equilibrium associated to a value of $V_a(-\mathbf{q}_I, \mathbf{0}) = 4k_{ap} > 0$. By continuity of V_a there exists a small enough neighborhood satisfying the hypotheses of Proposition 3 and the proof is completed. □

Remark 2. Our main result establishes *local* stability results rather than *global* ones. Two main obstructions motivate our local results. The first one arises from the fact that topological obstructions prevent a continuous feedback from inducing global robust stability properties in the attitude stabilization problem solved in Lemma 6 (where robustness is of the type commented in Remark 1). Alternative attitude stabilization solutions may be obtained following the hybrid approach proposed in Mayhew et al. (2009), among others. The second obstruction is related to the fact that, due to (25), our control law is not locally bounded when approaching the points in the state space where the controller state f is zero. While this is a well known and typical problem in UAV control, overcoming this limitation is less straightforward and could be addressed by following the hybrid approach in the recent work of Casau, Sanfelice, and Silvestre (2017). We emphasize here that both of the above limitations do not prevent large operating regions for our stabilizer: the attitude stabilization proof of Lemma 6 shows almost global results and the condition $f = 0$ is far from the typical operating conditions, due to the gravity action. The size of the operating region is well illustrated by the simulations carried out in Section 7 with large initial errors.

Remark 3 (*Restricted Orientation Stabilization*)**.** It is possible to extend the proposed solution with an additional requirement of restricted stabilization of a given *reference orientation* $\mathbf{q}_r \in \mathbb{S}^3$, where 'restricted' refers to the fact that such an orientation should be tracked with a lower hierarchical priority as compared to the translational error stabilization. This extended goal is achieved by first introducing the attitude error $\mathbf{q}'_\Delta \in \mathbb{S}^3$ defined as

$$\mathbf{q}'_\Delta := \mathbf{q}_r^{-1} \circ \mathbf{q}_d = \begin{bmatrix} \eta_r\eta_d + \boldsymbol{\epsilon}_r^\top\boldsymbol{\epsilon}_d \\ -\eta_d\boldsymbol{\epsilon}_r + \eta_r\boldsymbol{\epsilon}_d - [\boldsymbol{\epsilon}_r]_\times\boldsymbol{\epsilon}_d \end{bmatrix} = \begin{bmatrix} \eta'_\Delta \\ \boldsymbol{\epsilon}'_\Delta \end{bmatrix}, \tag{62}$$

and then replacing the expression of $\boldsymbol{\omega}_d$ in (25) using an additional term:

$$\boldsymbol{\omega}_d = \frac{1}{f}\,[\mathbf{d}_*]_\times\,\mathbf{R}(\mathbf{q}_d)^\top \boldsymbol{\nu} + \boldsymbol{\omega}'_d, \quad \text{with} \tag{63}$$

$$\boldsymbol{\omega}'_d = -k_q \mathbf{d}_* \mathbf{d}_*^\top \boldsymbol{\epsilon}'_\Delta, \tag{64}$$

where $k_q \in \mathbb{R}^+$ is a proportional gain. The projection $\mathbf{d}_*\mathbf{d}_*^\top$ in (64) ensures that $[\boldsymbol{\omega}'_d]_\times \mathbf{d}_* = 0$, so that the equalities in (46) remain unchanged and Fact 1 remains valid. As a consequence, the proofs in Lemma 3–6 are valid and Theorem 1 holds with (25) replaced by (64).

The appealing feature of using (63) instead of (25) is understood by looking at the Lyapunov-like function $V'_\Delta = 2(1+\eta'_\Delta)$, which is lower bounded. Since solutions converge to $\mathcal{Z}_0$, where $\boldsymbol{\nu} = \mathbf{0}$ and $\boldsymbol{\omega}_d = \boldsymbol{\omega}'_d$, using (23), (62), (63), restricting the attention to this set, we get

$$\begin{aligned}\dot{V}'_\Delta &= 2\dot{\eta}'_\Delta = (\boldsymbol{\epsilon}'_\Delta)^\top \boldsymbol{\omega}_d \\ &= -k_q (\boldsymbol{\epsilon}'_\Delta)^\top \mathbf{d}_* \mathbf{d}_*^\top \boldsymbol{\epsilon}'_\Delta = -k_q \|\mathbf{d}_*^\top \boldsymbol{\epsilon}'_\Delta\|^2,\end{aligned}$$

which, from lower boundedness of V'_Δ, implies that $\mathbf{d}_*^\top \boldsymbol{\epsilon}'_\Delta$ converges to zero, namely the projection of the orientation error $\boldsymbol{\epsilon}'_\Delta$ in the direction of $\mathbf{d}_*$ is zero. This extension is well illustrated by our simuations of Section 7.

7. Simulation results

The effectiveness of the proposed controller for solving Problem 1 is here validated by numerical simulations on the multi-rotor platform introduced in Ryll et al. (2019) characterized by $n = 6$ tilted propellers with fixed tilting angles, all sharing the same geometric and aerodynamics features (i.e., w.r.t. (8), $c_{f_i} = c_f$ and $c_{\tau_i} = c_\tau$, $i = 1 \dots 6$). This is depicted in Fig. 3.

To accurately describe the platform, we consider a local frame $\mathcal{F}_{P_i} = \{O_{P_i}, (\mathbf{x}_{P_i}, \mathbf{y}_{P_i}, \mathbf{z}_{P_i})\}$ for each rotor $i \in \{1 \dots 6\}$. The origin O_{P_i} coincides with the CoM of the ith motor–propeller combination, $\mathbf{x}_{P_i}, \mathbf{y}_{P_i} \in \mathbb{S}^2$ determine its spinning plane, while $\mathbf{z}_{P_i} \in \mathbb{S}^2$ identifies its spinning axis. As shown in Fig. 3, $O_{P_1} \dots O_{P_6}$ lie on the same plane where they are equally spaced on a circle, i.e., the considered multi-rotor is a *star-shaped hexarotor*. Formally, for $i \in \{1 \dots 6\}$, the position $\mathbf{p}_i \in \mathbb{R}^3$ of O_{P_i} in $\mathcal{F}_B$ is given by

$$\mathbf{p}_i = \mathfrak{q}(\gamma_i, \mathbf{e}_3) \circ \begin{bmatrix} 0 & \ell & 0 & 0 \end{bmatrix}^\top \circ \mathfrak{q}(\gamma_i, \mathbf{e}_3)^{-1}, \tag{65}$$

where, adopting (2), $\mathfrak{q}(\gamma_i, \mathbf{e}_3) \in \mathbb{S}^3$ is the unit quaternion associated to the rotation by $\gamma_i = (i-1)\pi/3$ about $\mathbf{e}_3$, according to the axis-angle representation given in Section 2, and $\ell > 0$ is the distance between O_{P_i} and O_B. Moreover, we assume that the orientation of each $\mathcal{F}_{P_i}$ w.r.t. $\mathcal{F}_B$ can be represented by the unit quaternion $\mathbf{q}_i \in \mathbb{S}^3$ such that

$$\mathbf{q}_i = \mathfrak{q}(\gamma_i, \mathbf{e}_3) \circ \mathfrak{q}(\beta_i, \mathbf{e}_2) \circ \mathfrak{q}(\alpha_i, \mathbf{e}_1), \tag{66}$$

where $\mathfrak{q}(\beta_i, \mathbf{e}_2), \mathfrak{q}(\alpha_i, \mathbf{e}_1) \in \mathbb{S}^3$ agree with the axis-angle representation and the constant tilt angles $\alpha_i, \beta_i \in (-\frac{\pi}{2}, \frac{\pi}{2}]$ uniquely define the direction of $\mathbf{z}_{P_i}$ in $\mathcal{F}_B$. Indeed, the frame $\mathcal{F}_{P_i}$ is obtained from $\mathcal{F}_B$ by first rotating by α_i about x-axis and then by β_i around the resulting y-axis. In particular, these angles are chosen so that $\alpha_i = -\alpha_{i+1}$ and $\alpha_i = \frac{\pi}{6}$ for $i = 1, 3, 5$, while $\beta_i = \frac{\pi}{18}$ for $i = 1 \dots 6$. Since the tilting is fixed, all angles α_i and β_i, $i = 1, \dots, 6$, are constant during the flight.

The described hexarotor, whose physical and aerodynamic parameters are summarized in Table 1, satisfies Assumption 1, and the associated matrix $\mathbf{K}$ in (19) is not simply the identity matrix. In particular, $\mathbf{K}$ can be chosen as the product between an orthogonal basis of the null space of $\mathbf{F}$ and its transpose (i.e., $\mathbf{K} = \bar{\mathbf{F}}(\bar{\mathbf{F}})^\top$ as in the proof of Lemma 1).

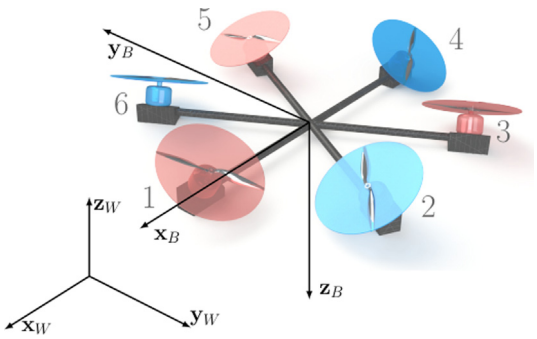

Fig. 3. Star-shaped hexarotor with tilted propellers described in Section 7 - red/blue discs correspond to CW/CCW rotors.

Table 1
Physical and aerodynamic parameters of the hexarotor.

c_f	c_τ	ℓ	m	J
$10^{-5}\ \frac{\text{N}}{\text{Hz}^2}$	$10^{-7}\ \frac{\text{N}}{\text{Hz}^2}$	0.5 m	1.5 kg	diag{[0.075 0.075 0.15]} kg m^2

Table 2
Standard deviation of the modeled sensor noise added to the corresponding physical quantities.

$\mathbf{p}$	$\mathbf{v}$	$\mathbf{q}$	$\boldsymbol{\omega}$
6.4×10^{-4} m	1.4×10^{-3} m/s	1.2×10^{-3}	2.7×10^{-3} rad/s

The performed simulations use dynamics (12)(a)–(12)(d) augmented with several unmodeled real-world effects, which should be well handled by the control scheme because of the robustness properties emphasized in Remark 1.

- The position and orientation feedback and their derivatives are affected by time delay $t_f = 0.012$ s and Gaussian noise corrupts the measurements according to Table 2. The actual position and orientation are fed back with a lower sampling frequency of 100 Hz while the controller runs at 500 Hz. These properties are reflecting a typical motion capture system and an inertial measurement unit (IMU).
- The electronic speed controller (ESC) driving the motors is modeled by quantizing the desired input $\mathbf{u}$ via a 10 bit discretization in the feasible motor speed, thus resulting in a step size of ≈ 0.12 Hz. Additionally, the motor–propeller combination is modeled as a first order transfer function $\big(G(s) = (1 + 0.005s)^{-1}\big)$. The resulting signal is corrupted by a rotational velocity dependent Gaussian noise (see Table 2). This combination reproduces quite accurately the dynamic behavior of a common ESC motor–propeller combination, such as BL-Ctrl-2.0, by MikroKopter, Robbe ROXXY 2827-35 and a 10 inch rotor blade (Franchi & Mallet, 2017).

To well illustrate the proposed control scheme, in the following we report the results of a simulation composed of three phases. The first phase ([0, 10]s) corresponds to the take off maneuver during which the platform is required to lift up from the ground starting from its initial position (the origin of the world frame). During the second phase ([10, 20]s), the control goal is to steer the vehicle to a new reference position without imposing any reference orientation. Finally, in the third phase ([20, 30]s), the platform stabilizes a specific orientation (according to the developments of Remark 3), while maintaining the achieved position.

To accomplish the described tasks sequence, two different preferential directions are imposed: in the first phase we select $\mathbf{d}_* = \mathbf{e}_3$ since a vertical force is needed for the take off maneuver,

in both the second and third phase, instead, the preferential direction is chosen so that the vehicle is required to hover with a tilting of $\frac{\pi}{18}$ w.r.t. the x-axis of the world frame (identified by the unit vector $\mathbf{x}_W \in \mathbb{S}^2$ in Fig. 3). This last scenario might occur, for instance, in environmental inspection applications wherein the employed aerial vehicle is equipped with a rigidly attached end effector (Ollero et al., 2018). The gains of the controller are chosen as $k_{pp} = 12$, $k_{pd} = 8$, $k_{ap} = 5$, $k_{ad} = 2.5$, $k_\Delta = 1.3$ and $k_q = 0$ for the first two phases, $k_q = 1$ in the third one. These values induce desirable transients on the equivalent PD-like error dynamics. Furthermore, note that $\boldsymbol{\omega}_d$ accounts for the additional term $\boldsymbol{\omega}_d'$ in (64) only when $k_q \neq 0$, i.e., only during the third phase when a specific reference orientation is imposed.

The simulation results are depicted in Fig. 4. The first and second plots report the position and orientation of the hexarotor, respectively, compared to their reference values. We emphasize that $\mathbf{q}_r$ coincides with $\mathbf{q}_d$ during phases 1 and 2, when a reference orientation is not imposed. The trend of the error variables $\mathbf{q}_\Delta$, $\boldsymbol{\omega}_\Delta$, $\mathbf{e}_p$ and $\mathbf{e}_v$ is depicted in the subsequent four plots. The seventh plot reports the controller state f, compared to its equilibrium value mg (dashed). Finally, the last plot shows the control inputs commanded to the propellers. Note that we use the roll-pitch-yaw (RPY) angles $(\phi_\bullet, \theta_\bullet, \psi_\bullet)$ to represent the attitude to give a better insight of the vehicle attitude, however the internal computations are all carried out with unit quaternions.

During the take-off (first) phase, the hexarotor smoothly reaches the reference position in roughly 5 s, while maintaining a constant orientation. Note that take-off happens after almost 1 s from the beginning of the simulation because the controller state f (seventh plot) is initialized at $\frac{1}{2}mg$, and the equilibrium value mg needs to be reached to counteract the gravity force, thereby enabling take-off. In general it is advisable to initialize the controller state to $\mathbf{q}_d(0) = \mathbf{q}(0)$ and $f(0) = mg$, to minimize the transients, but we deliberately select large initial errors in our simulations to validate the closed-loop performance with non-ideal controller initializations. In the second phase, the selected zero-moment direction $\mathbf{d}_*$ induces a rotation of the platform whose roll angle ϕ quickly sets to $\frac{\pi}{18}$, as shown in the second plot. At the same time, the vehicle is required to track a new position by moving on the (xy)-plane of the world frame. The position error $\mathbf{e}_p$ (shown in the fifth plot) converges to zero in roughly 5 s, similar to the first phase, since the controller gains are unchanged. From the third plot we also observe that the position and attitude errors converge with comparable transient time scales, a feature that is not allowed in two-loops control schemes requiring time-scale separation between position and attitude transients. Finally, one can notice that the second phase of the conducted simulation is also marked by a different distribution of the propellers command inputs. The two propellers whose CoMs lie on the rotation axis, namely rotors 1 and 4 in Fig. 3, are, indeed, required to decrease their spinning rates. Nonetheless, at the steady-state, all the spinning rates belong to [60, 110]Hz, which represents a feasible range of values from a technological point of view. Finally, in the third phase, the proposed controller, extended as in Remark 3, guarantees the stabilization of the vehicle to the given reference orientation $(\phi_r, \theta_r, \psi_r) = \left(\frac{\pi}{18}, 0, \frac{\pi}{4}\right)$, which coincides with a rotation about the preferential direction and justifies the fact that $\mathbf{q}_\Delta = \mathbf{q}_r^{-1} \circ \mathbf{q}$ converges to zero. Remarkably, this maneuver does not modify the steady-state propeller inputs.

In our last simulation we illustrate the comments in Remark 2 by using the same position reference as in phase 2 of the previous simulation, but starting from large initial attitude errors, which also cause large position transients, due to the cascaded structure of the error dynamics. Fig. 5 reports the RPY angles associated to the orientation error $\mathbf{q}_\Delta$, the position error $\mathbf{e}_p$, the controller state

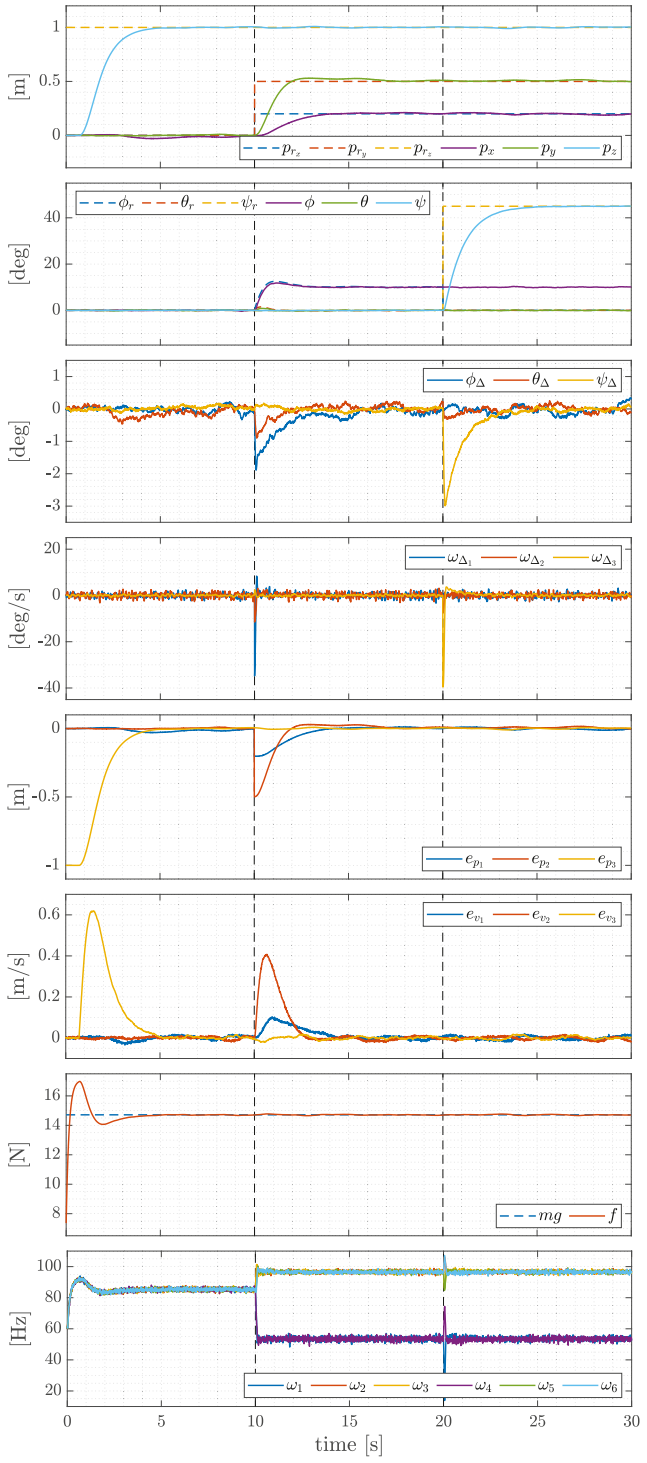

Fig. 4. The three phases in Section 7: take off in [0, 10]s, hovering in [10, 20]s and orientation stabilization in [20, 30]s.

f and the spinning rate ω_i of the platform propellers for multiple selections of the initial attitude. In particular, the initial angles $(\phi_0, \theta_0, \psi_0)$ associated to $\mathbf{q}_0 = \mathbf{q}(0)$ are chosen with $\psi_0 = 0$ and (ϕ_0, θ_0) assuming multiple values (reported in the legend) in the set $\left\{-\frac{\pi}{3}, 0, \frac{\pi}{3}\right\} \times \left\{-\frac{\pi}{3}, 0, \frac{\pi}{3}\right\}$. In all of the considered cases both the position and orientation error converge to zero in less than 10 s with smooth transients. The large overshoots reveal that, as anticipated in Remark 2, the region of attraction associated to our

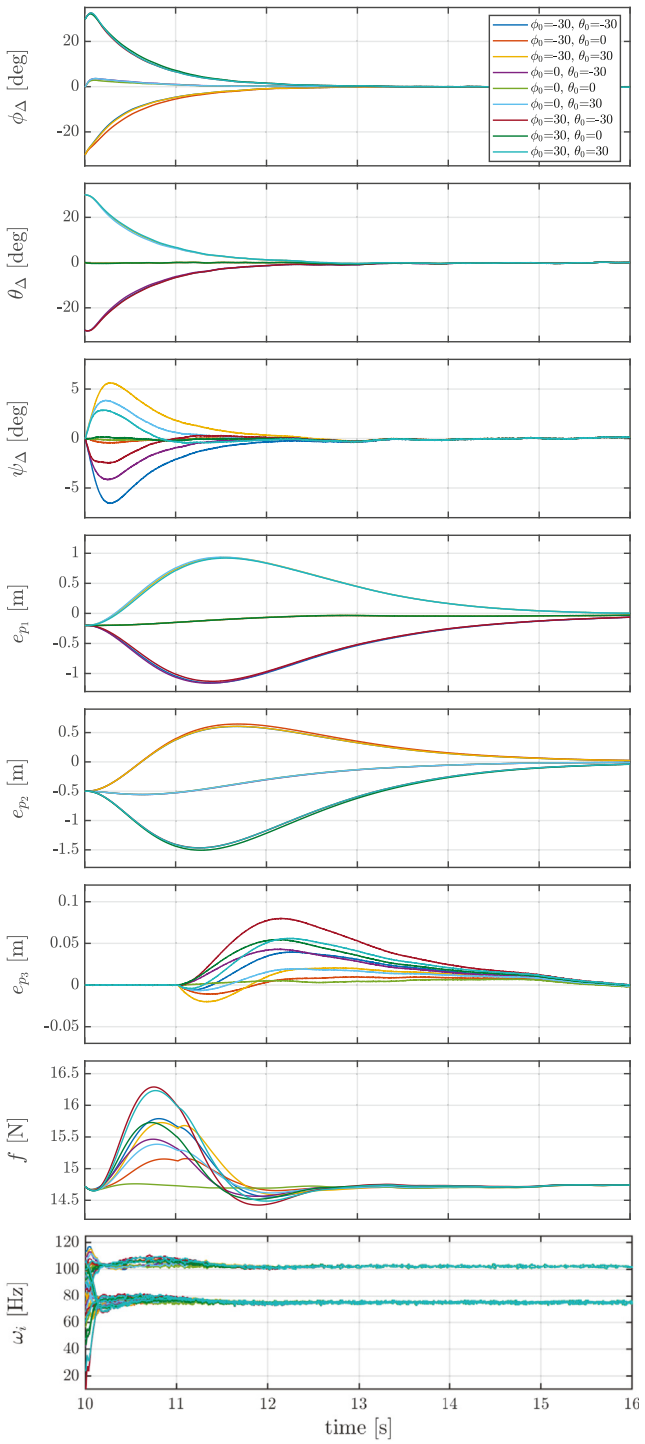

Fig. 5. Second phase of the simulation of Fig. 4 with different attitude initial conditions.

local asymptotic stability proofs of Section 6 is rather large. In addition, we observe that the rotor commands are in the feasible spinning rate range in all the cases.

8. Conclusions

We addressed the hovering control task for a generic class of multi-rotor aerial vehicles (MAV) whose propellers are arbitrary in number and position/orientation. Adopting the quaternion attitude representation, we designed a state feedback nonlinear controller to stabilize the MAV at a reference position with an arbitrary but constant orientation. The proposed solution relies on some non-restrictive assumptions on the control input matrices $\mathbf{F}$ and $\mathbf{M}$ that ensure the existence of a preferential direction in the feasible force space, along which the control force and the control moment are decoupled. Stability and asymptotic convergence of the tracking error have been rigorously proven through a cascaded-like proof exploiting nested sets and reduction theorems. The theoretical findings are confirmed by the numerical simulation results, supporting the test of the control scheme on a real platform in the near future.

Appendix. Proof of the identity $\dot{\boldsymbol{\omega}}_d = \boldsymbol{\omega}_{dd}$

The identity $\dot{\boldsymbol{\omega}}_d = \boldsymbol{\omega}_{dd}$ stated in Section 5 is proven below using $[[\boldsymbol{\epsilon}_1]_\times \boldsymbol{\epsilon}_2]_\times = [\boldsymbol{\epsilon}_1]_\times [\boldsymbol{\epsilon}_2]_\times - [\boldsymbol{\epsilon}_2]_\times [\boldsymbol{\epsilon}_1]_\times = \boldsymbol{\epsilon}_2 \boldsymbol{\epsilon}_1^\top - \boldsymbol{\epsilon}_1 \boldsymbol{\epsilon}_2^\top$. The derivative of $\boldsymbol{\omega}_d$ in (25) results from the sum of three components, namely $\dot{\boldsymbol{\omega}}_d = \dot{\boldsymbol{\omega}}_{d,1} + \dot{\boldsymbol{\omega}}_{d,2} + \dot{\boldsymbol{\omega}}_{d,3}$ with

$$\dot{\boldsymbol{\omega}}_{d,1} = -\frac{1}{f^2}[\mathbf{d}_*]_\times \mathbf{R}_d^\top \boldsymbol{\nu} \dot{f} \overset{(26)}{=} -\frac{1}{f^2}[\mathbf{d}_*]_\times \mathbf{R}_d^\top \boldsymbol{\nu} \mathbf{d}_*^\top \mathbf{R}_d^\top \boldsymbol{\nu}$$
$$= -\frac{\left(\mathbf{d}_*^\top \mathbf{R}_d^\top \boldsymbol{\nu}\right)}{f^2}[\mathbf{d}_*]_\times \mathbf{R}_d^\top \boldsymbol{\nu}$$

$$\dot{\boldsymbol{\omega}}_{d,2} = \frac{1}{f}[\mathbf{d}_*]_\times \dot{\mathbf{R}}_d^\top \boldsymbol{\nu} = -\frac{1}{f}[\mathbf{d}_*]_\times [\boldsymbol{\omega}_d]_\times \mathbf{R}_d^\top \boldsymbol{\nu}$$
$$\overset{(25)}{=} -\frac{1}{f^2}[\mathbf{d}_*]_\times \left[[\mathbf{d}_*]_\times \mathbf{R}_d^\top \boldsymbol{\nu}\right]_\times \mathbf{R}_d^\top \boldsymbol{\nu}$$
$$= -\frac{\left(\mathbf{d}_*^\top \mathbf{R}_d^\top \boldsymbol{\nu}\right)}{f^2}[\mathbf{d}_*]_\times \mathbf{R}_d^\top \boldsymbol{\nu}$$

where $\mathbf{R}_d^\top$ stands for $\mathbf{R}^\top(\mathbf{q}_d)$. Thus, we get

$$\dot{\boldsymbol{\omega}}_{d,1} + \dot{\boldsymbol{\omega}}_{d,2} = -\frac{2}{f^2}\left(\mathbf{d}_*^\top \mathbf{R}_d^\top \boldsymbol{\nu}\right)[\mathbf{d}_*]_\times \mathbf{R}_d^\top \boldsymbol{\nu}, \tag{A.1}$$
$$= -\frac{1}{f}\kappa(\mathbf{e}_p, \mathbf{e}_v, \mathbf{f}_\Delta)[\mathbf{d}_*]_\times \mathbf{R}_d^\top \boldsymbol{\nu}, \tag{A.2}$$

by introducing the gain $\kappa(\mathbf{e}_p, \mathbf{e}_v, \mathbf{f}_\Delta) \in \mathbb{R}$ that, exploiting (27), results as in (35). The derivation of $\dot{\boldsymbol{\omega}}_{d,3}$ is instead reported in (A.3)–(A.7) where $\mathbf{R}_d = \mathbf{R}(\mathbf{q}_d)$ and $\mathbf{R} = \mathbf{R}(\mathbf{q})$ to simplify the notation.

$$\dot{\boldsymbol{\omega}}_{d,3} = \frac{1}{\xi f}[\mathbf{d}_*]_\times \mathbf{R}_d^\top \dot{\boldsymbol{\nu}}$$
$$\overset{(27)}{=} \frac{1}{\xi f}[\mathbf{d}_*]_\times \mathbf{R}^\top(\mathbf{q}_d)\left(\frac{k_{pd}k_{pp}}{m}\dot{\mathbf{e}}_p + \left(\frac{k_{pd}^2}{m} - k_{pp}\right)\dot{\mathbf{e}}_v - \left(\frac{k_{pd}}{m} + k_\Delta\right)\dot{\mathbf{f}}_\Delta\right) \tag{A.3}$$

$$\overset{(40)}{=} \frac{1}{\xi f}[\mathbf{d}_*]_\times \mathbf{R}_d^\top \left(\frac{k_{pd}k_{pp}}{m}\mathbf{e}_v - \left(\frac{k_{pd}}{m} + k_\Delta\right)\dot{\mathbf{f}}_\Delta + \left(\frac{k_{pd}^2}{m^2} - \frac{k_{pp}}{m}\right)\left(-mg\mathbf{e}_3 + (\mathbf{R} - \mathbf{R}_d\mathbf{d}_*\xi f + \mathbf{f}_r + \mathbf{f}_\Delta)\right)\right) \tag{A.4}$$

$$= \frac{1}{\xi f}[\mathbf{d}_*]_\times \mathbf{R}_d^\top \left(\frac{k_{pd}k_{pp}}{m}\mathbf{e}_v - \left(\frac{k_{pd}}{m} + k_\Delta\right)\dot{\mathbf{f}}_\Delta\right.$$

$$+\left(\frac{k_{pd}^2}{m^2}-\frac{k_{pp}}{m}\right)\left(-mg\mathbf{e}_3+\mathbf{R}\mathbf{d}_*\xi f+\mathbf{f}_r+\mathbf{f}_\Delta\right)\Bigg) \tag{A.5}$$

$$\overset{(22)}{=}\frac{1}{\xi f}[\mathbf{d}_*]_\times\mathbf{R}_d^\top\left(\frac{k_{pd}k_{pp}}{m}\mathbf{e}_v-\left(\frac{k_{pd}}{m}+k_\Delta\right)\dot{\mathbf{f}}_\Delta\right.$$
$$\left.+\left(\frac{k_{pd}^2}{m^2}-\frac{k_{pp}}{m}\right)\left(\mathbf{R}\mathbf{d}_*\xi f-k_{pp}\mathbf{e}_p-k_{pd}\mathbf{e}_v+\mathbf{f}_\Delta\right)\right) \tag{A.6}$$

$$\overset{(41)}{=}\frac{1}{\xi f}[\mathbf{d}_*]_\times\mathbf{R}_d^\top\left(\frac{k_{pd}k_{pp}}{m}\mathbf{e}_v+\left(\frac{k_{pd}}{m}+k_\Delta\right)k_\Delta\mathbf{f}_\Delta\right.$$
$$\left.+\left(\frac{k_{pd}^2}{m^2}-\frac{k_{pp}}{m}\right)\left(\mathbf{R}\mathbf{d}_*\xi f-k_{pp}\mathbf{e}_p-k_{pd}\mathbf{e}_v+\mathbf{f}_\Delta\right)\right) \tag{A.7}$$

Using (A.2) and (A.7), and setting $k_1, k_2(\mathbf{e}_p, \mathbf{e}_v, \mathbf{f}_\Delta), k_3(\mathbf{e}_p, \mathbf{e}_v, \mathbf{f}_\Delta)$ and $k_4(\mathbf{e}_p, \mathbf{e}_v, \mathbf{f}_\Delta)$ as in (31)–(34), it is straightforward to verify that $\dot{\boldsymbol{\omega}}_d = \boldsymbol{\omega}_{dd}$.

References

Abci, B., Zheng, G., Efimov, D., & El Najjar, M. E. B. (2017). Robust altitude and attitude sliding mode controllers for quadrotors. *IFAC-PapersOnLine*, *50*(1), 2720–2725.

Alkhoori, F., Safwan, S. B., Zweiri, Y., Sahinkaya, M. N., & Seneviratne, L. (2017). PID-LQR controllers for quad-rotor hovering mode. In *IEEE international conference on systems and informatics* (pp. 50–54).

Antonello, A., Michieletto, G., Antonello, R., & Cenedese, A. (2018). A dual quaternion feedback linearized approach for maneuver regulation of rigid bodies. *IEEE Control Systems Letters*, *2*(3), 327–332.

Carrillo, L., Dzul, A., & Lozano, R. (2012). Hovering quad-rotor control: A comparison of nonlinear controllers using visual feedback. *IEEE Transactions on Aerospace and Electronic Systems*, *48*(4), 3159–3170.

Casau, P., Sanfelice, R., & Silvestre, C. (2017). Hybrid stabilization of linear systems with reverse polytopic input constraints. *IEEE Transactions on Automatic Control*, *62*(12), 6473–6480.

Chen, F., Jiang, R., Zhang, K., Jiang, B., & Tao, G. (2016). Robust backstepping sliding-mode control and observer-based fault estimation for a quadrotor UAV. *IEEE Transactions on Industrial Electronics*, *63*(8), 5044–5056.

Choi, Y.-C., & Ahn, H.-S. (2015). Nonlinear control of quadrotor for point tracking: Actual implementation and experimental tests. *IEEE/ASME Transactions on Mechatronics*, *20*(3), 1179–1192.

Diebel, J. (2006). Representing attitude: Euler angles, unit quaternions, and rotation vectors. *Matrix*, *58*(15–16), 1–35.

El-Hawwary, M. I., & Maggiore, M. (2013). Reduction theorems for stability of closed sets with application to backstepping control design. *Automatica*, *49*(1), 214–222.

Franchi, A., Carli, R., Bicego, D., & Ryll, M. (2018). Full-pose tracking control for aerial robotic systems with laterally bounded input force. *IEEE Transactions on Robotics*, *34*(2), 534–541.

Franchi, A., & Mallet, A. (2017). Adaptive closed-loop speed control of BLDC motors with applications to multi-rotor aerial vehicles. In *IEEE international conference on robotics and automation* (pp. 5203–5208).

Fuhrmann, M., & Horowitz, M. C. (2017). Droning on: Explaining the proliferation of unmanned aerial vehicles. *International Organization*, *71*(2), 397–418.

Goebel, R., Sanfelice, R. G., & Teel, A. R. (2012). *Hybrid dynamical systems: Modeling, stability, and robustness*. Princeton University Press.

Goodarzi, F. A., & Lee, T. (2017). Global formulation of an extended Kalman filter on SE(3) for geometric control of a quadrotor UAV. *Journal of Intelligent and Robotic Systems*, *88*(2–4), 395–413.

Hayat, S., Yanmaz, E., Brown, T. X., & Bettstetter, C. (2017). Multi-objective UAV path planning for search and rescue. In *IEEE international conference on robotics and automation* (pp. 5569–5574).

Hua, M.-D., Hamel, T., Morin, P., & Samson, C. (2013). Introduction to feedback control of underactuated VTOL vehicles: A review of basic control design ideas and principles. *IEEE Control Systems Magazine*, *33*(1), 61–75.

Invernizzi, D., & Lovera, M. (2017). Geometric tracking control of a quadcopter tiltrotor UAV. *IFAC-PapersOnLine*, *50*(1), 11565–11570.

Kim, H., Mokdad, L., & Ben-Othman, J. (2018). Designing UAV surveillance frameworks for smart city and extensive ocean with differential perspectives. *IEEE Communications Magazine*, *56*(4), 98–104.

Kuipers, J. B. (2002). *Quaternions and rotation sequences: A primer with applications to orbits, aerospace and virtual reality, vol. 66*. Princeton University Press.

Lee, T., Leoky, M., & McClamroch, N. (2010). Geometric tracking control of a quadrotor UAV on SE(3). In *IEEE conference on decision and control* (pp. 5420–5425).

Liu, C., Pan, J., & Chang, Y. (2016). PID and LQR trajectory tracking control for an unmanned quadrotor helicopter: Experimental studies. In *IEEE Chinese control conference* (pp. 10845–10850).

Loianno, G., Spurny, V., Thomas, J., Baca, T., Thakur, D., Hert, D., et al. (2018). Localization, grasping, and transportation of magnetic objects by a team of MAVs in challenging desert like environments. *IEEE Robotics and Automation Letters*, *3*(3), 1576–1583.

Lotufo, M. A., Colangelo, L., Perez-Montenegro, C., Novara, C., & Canuto, E. (2016). Embedded model control for UAV quadrotor via feedback linearization. *IFAC-PapersOnLine*, *49*(17), 266–271.

Maggiore, M., Sassano, M., & Zaccarian, L. (2019). Reduction theorems for hybrid dynamical systems. *IEEE Transactions on Automatic Control*, *64*(6), 2254–2265.

Mayhew, C., Sanfelice, R., & Teel, A. (2009). Robust global asymptotic attitude stabilization of a rigid body by quaternion-based hybrid feedback. In *IEEE conference on decision and control* (pp. 2522–2527).

Michieletto, G., Cenedese, A., Zaccarian, L., & Franchi, A. (2017). Nonlinear control of multi-rotor aerial vehicles based on the zero-moment direction. *IFAC-PapersOnLine*, *50*(1), 13144–13149.

Michieletto, G., Ryll, M., & Franchi, A. (2017). Control of statically hoverable multi-rotor aerial vehicles and application to rotor-failure robustness for hexarotors. In *IEEE international conference on robotics and automation* (pp. 2747–2752).

Michieletto, G., Ryll, M., & Franchi, A. (2018). Fundamental actuation properties of multi-rotors: Force-moment decoupling and fail-safe robustness. *IEEE Transactions on Robotics*, *34*(3), 702–715.

Motlagh, N. H., Bagaa, M., & Taleb, T. (2017). UAV-based IoT platform: A crowd surveillance use case. *IEEE Communications Magazine*, *55*(2), 128–134.

Ollero, A., Heredia, G., Franchi, A., Antonelli, G., Kondak, K., Sanfeliu, A., et al. (2018). The AEROARMS project: Aerial robots with advanced manipulation Capabilities for inspection and maintenance. In *Floating-base (aerial and underwater) manipulation IEEE Robotics and Automation Magazine*, *25*, 12–23 (Special issue).

Ruggiero, F., Lippiello, V., & Ollero, A. (2018). Aerial manipulation: A literature review. *IEEE Robotics and Automation Letters*, *3*(3), 1957–1964.

Ryll, M., Muscio, G., Pierri, F., Cataldi, E., Antonelli, G., Caccavale, F., et al. (2019). 6D interaction control with aerial robots: The flying end-effector paradigm. *International Journal of Robotics Research*, *38*(9), 1045–1062.

Sandiwan, A. P., Cahyadi, A., & Herdjunanto, S. (2017). Robust proportional-derivative control on SO(3) with disturbance compensation for quadrotor UAV. *International Journal of Control, Automation and Systems*, *15*(5), 2329–2342.

Seuret, A., Prieur, C., Tarbouriech, S., Teel, A., & Zaccarian, L. (2019). A nonsmooth hybrid invariance principle applied to robust event-triggered design. *IEEE Transactions on Automatic Control*, *64*(5), 2061–2068.

Shakhatreh, H., Sawalmeh, A. H., Al-Fuqaha, A., Dou, Z., Almaita, E., Khalil, I., et al. (2019). Unmanned aerial vehicles: A survey on civil applications and key research challenges. *IEEE Access*, *7*, 48572–48634.

Spurnỳ, V., Báča, T., Saska, M., Pěnička, R., Krajník, T., Thomas, J., et al. (2019). Cooperative autonomous search, grasping, and delivering in a treasure hunt scenario by a team of unmanned aerial vehicles. *Journal of Field Robotics*, *36*(1), 125–148.

Tang, S., & Kumar, V. (2018). Autonomous flying. *Annual Review of Control, Robotics, and Autonomous Systems*, *1*(1), 29–52.

Tian, Y. (2004). Rank equalities for block matrices and their Moore-Penrose inverses. *Houston Journal of Mathematics*, *30*(4), 483–510.

Zhang, F. (2011). *Matrix theory: basic results and techniques*. Springer Science & Business Media.

Giulia Michieletto received the M.S. (2014) and the Ph.D. (2018) degrees from the University of Padova, Italy, where she is currently Assistant Professor with the Department of Management and Engineering. From March 2016 to February 2017, she was a Visiting Researcher at LAAS-CNRS, Toulouse, France. From February 2018 to November 2019, she was a post-doc fellow with the SPARCS group at the Department of Information Engineering, University of Padova, Italy. Her main research interests include multi-agent systems modeling and control with a special regard to networked formations of aerial vehicles and nano satellites.

Angelo Cenedese received the M.S. (1999) and the Ph.D. (2004) degrees from the University of Padova, Italy, where he is currently an Associate Professor with the Department of Information Engineering and leader of the SPARCS research group. He has held several visiting positions at the UKAEA-JET laboratories in the Culham Research Centre (UK), the UCLA Vision Lab (CA-USA), the F4E European Agency (Spain). His research interests include system modeling, control theory and its applications, sensor and actuator networks, multi agent systems. On these subjects, he has published more than 150 papers and holds three patents.

Luca Zaccarian received the Ph.D. from the University of Roma Tor Vergata (Italy) in 2000, where he became assistant and then associate professor. Since 2011 he is Directeur de Recherche at the LAAS-CNRS, Toulouse (France) and since 2013 he holds a part-time associate professor position at the University of Trento, Italy. Luca Zaccarian's main research interests include analysis and design of nonlinear and hybrid control systems, modeling and control of mechatronic systems. He was a recipient of the 2001 O. Hugo Schuck Best Paper Award given by the American Automatic Control Council. He is a fellow of the IEEE, class of 2016.

Antonio Franchi is an Associate Professor in the Faculty of Electrical Engineering, Mathematics & Computer Science, at the University of Twente, Enschede, The Netherlands, and an Associate Researcher at LAAS-CNRS, Toulouse, France. His main research interests include the design and control for robotic systems with applications to multi-robot systems and aerial robots. He co-authored more than 130 papers in peer-reviewed international journals and conferences. He is an IEEE Senior Member. Since 2012 he has been serving in the editorial board of the major IEEE robotics conferences and journals, including the IEEE Transactions on Robotics. He is the co-founder and co-chair of the IEEE RAS Technical Committee on Multiple Robot Systems.